OFF-GRID MEMS SENSORS CONFIGURATIONS FOR TRANSPORTATION APPLICATIONS

Prepared by:

Alivia Plankis, Graduate Research Assistant
Paul Heyliger, Professor

Department of Civil and Environmental Engineering
Colorado State University
Fort Collins, Colorado 80523

October 2013

Acknowledgements

The funding for this research was provided by a grant from Mountain Plains Consortium (MPC). This support is gratefully acknowledged.

Disclaimer

EXECUTIVE SUMMARY

The worsening problem of aging and deficient infrastructure in this nation and across the world has demonstrated the need for an improved system to monitor and maintain these structures. The field of structural health monitoring has grown in recent years to address this issue. The goal of this field is to continually monitor the condition of a structure to detect and mitigate damage that may occur. Many structural health monitoring methods have been developed and most of these require sensor systems to collect the necessary information to assess the current strength and integrity of a structure. The motivation for this report is a proposed new microelectromechanical systems (MEMS) sensor with applications in civil infrastructure sensing. The work required was to determine accurate estimates of the resonant frequencies for a fixed-fixed silicon bridge within the device so that further testing and development could proceed. Additional knowledge and information were essential, though, before these requested calculations could be performed confidently. First, a thorough review of current structural health monitoring concepts and methods was performed to better understand the field in which this device would be applied and what incentive existed to develop a new sensor. Second, an in-depth investigation of vibrational beam mechanics theories was completed to ensure the accuracy of the frequency results for the new MEMS sensor. This report analyzed the influence of three assumptions employed in the Euler-Bernoulli, Rayleigh, and Timoshenko beam theories by comparing their results to a three-dimensional, elasticity-based approximation for vibrational frequencies and mode shapes. The results of this report showed that all three theories are insufficient when a fixed support is involved, so the elasticity-based approximation was utilized to calculate the frequencies for the bridge component in the MEMS device. These results have been passed on to the developers so that the testing process could move forward in the hopes that the device could advance the field of structural health monitoring in the future.

TABLE OF CONTENTS

LIST OF TABLES

LIST OF FIGURES

1. INTRODUCTION

The issue of aging infrastructure in this country has become apparent to the engineering community in recent years due to catastrophic failures, such as the collapse of the I-35W Bridge across the Mississippi River in Minneapolis, MN, and also from an increasing awareness of the current state of structural health. Recent structural surveys have shown more than a quarter of the nation's bridges to be structurally deficient or obsolete and have brought to attention the fact that more than a third have been in service for more than 40 years [1, 2]. This data, along with the occurrence of major failures, has demonstrated the necessity for methods in which to detect structural damage and properly prioritize the replacement of existing bridges and buildings. A notable field which has developed to answer this need is that of structural health monitoring. The basic concept behind this field is that by continually tracking the strength and integrity of a structure, damage can be detected, the life span can be assessed, and proper maintenance and mitigation actions taken. In order to perform most structural health monitoring methods, sensors are required to collect data on the key parameters involved in evaluating a structure's state of strength. Numerous devices have been developed and applied for this purpose, but several advancements still need to be made before structural health monitoring methods can be prevalently applied in an accurate and cost-efficient manner.

The motivation behind this report is a proposed new microelectromechanical systems (MEMS) sensor with applications in monitoring civil infrastructure, which could help address some of the deficiencies with current sensor technologies. A thin fixed-fixed silicon bridge provides the primary sensing element in this device. As the sensor is loaded, the resonant frequency of the bridge will change and provide information about the component to which it is attached. The key goal of this report was to investigate the properties of this bridge by performing calculations for certain modal frequencies, which are needed before further development can proceed. Before successfully executing the requested analysis, additional understanding was essential. To better comprehend the incentive for the invention and development of a new sensor, a review of current structural health monitoring methods and the technologies utilized for them was conducted. Also, to ensure more accurate frequency results, an in-depth vibrational mechanics study was completed to determine the effectiveness of common beam theories for varying support conditions. The remainder of this chapter will layout the objectives of each of these sections, how they were obtained, and the organization of the paper.

1.1 Objectives

This study contains three main goals which are all connected but each have their own objectives. The goal that was the impetus for this research was to determine accurate modal frequencies for the silicon bridge within the proposed MEMS sensor. The details and methods for this goal will be discussed last because the completion of the other two sections of this study was necessary before this goal could be achieved.

The first basic goal for this study was to obtain a greater understanding of the field of structural health monitoring through a review of concepts, methods, and sensors. With the knowledge gained from this research, the motivation for a new sensor could be recognized and thus provide defense for the relevance of the calculations for the new MEMS sensor. A number of objectives were created to ensure that this study of structural health monitoring was successful and adequate information was gained. These objectives are:

1. Ascertain the primary goals of the practice of structural health monitoring
2. Identify common methods that have been developed to attain these goals
3. Explain the concepts behind each of these methods, as well as both the benefits and drawbacks associated with their use
4. Establish what types of sensors are available or in development to collect the necessary data for these structural health monitoring methods to be effective

5. Describe the theory of operation for these sensors, how they are applicable, and any advantages or disadvantages they may possess

The objectives provided were achieved by a process of thorough research of reference books, journal articles, academic reports, and more. The topic of this research was at first very broad, covering the basics of structural health monitoring, and was continually refined as greater detail of methods and sensors became of interest. The amount of information available is immense, so the review created is not comprehensive. However, the material found and discussed provided a sufficient knowledge base to move forward with the calculations for the suggested new sensor, and possibly provide aid for others who may continue the development and research for this and other similar devices.

The second leading goal of this study was to perform a vibrational mechanics study, the results of which could be used to ensure the accuracy of the frequency calculations for the MEMS device. This vibration study considered three commonly used beam mechanics theories: Euler-Bernoulli, Rayleigh, and Timoshenko. These three models increase in complexity, but all contain common assumptions to simplify analysis procedures. The purpose of this investigation was to determine how three of these common assumptions affect the accuracy of frequency and mode shape calculations. In order to achieve this, a more accurate three-dimensional elasticity approximation was utilized. The following objectives were conceived to carry out this study effectively.

1. Present the theory behind each of the common beam models and the displacement effects which are included or ignored in each
2. Provide a list of the common assumptions included in all three of the discussed beam theories
3. Explain the three-dimensional elasticity approximation concepts and its development
4. Investigate the effects of three of the basic assumptions: high slenderness, isotropic material properties, and the idea that the Poisson effect is negligible
5. Analyze and discuss if and when each of the three common beam theories are applicable based on the calculations

A number of steps were taken to accomplish these objectives. First, computational programs, which had been provided from previous research, were modified to produce frequency calculations for each of the beam theories and the elasticity solution when applied to three different support cases: fixed-free, fixed-fixed, and simply-supported. Once these were prepared, various calculations were performed to allow for the investigation of the three assumptions of interest. Varying beam lengths were employed to study slenderness, and two sets of material properties were applied to research the effect of anisotropy. Lastly, the more accurate elasticity-based solution was utilized for calculations both with and without the Poisson ratio included to better isolate this effect. The conclusions determined about the accuracy of common beam theories from this vibrational mechanics study were applied to the calculations performed on the fixed-fixed bridge of the MEMS sensor.

The final goal of determining accurate vibrational frequency estimates for the new MEMS sensor was possible after the knowledge gained from the previous two goals was applied. The more accurate three-dimensional elasticity-based approximation method was employed for the frequency calculations. Accurate results were obtained for varying bridge lengths and passed on to the developers of the device. The main objective of this section was to provide valuable information to allow for further development and research to proceed for this new and promising device.

1.2 Report Layout

The information for the three goals of this study has been organized into the four remaining sections. Section 2 presents the results of the structural health monitoring review. It covers two categories of possible methods, with specific examples for each of them, and which are explained and compared. The types of sensors which are available are then explained and discussed. The information provides a thorough understanding of the field of structural health monitoring, how it is currently performed, and what improvements can be made.

In Section 3, all the concepts and development of the three beam theories to be studied and the proposed full elasticity based solution are explained. The mechanics effects, which are included in each of them, are presented, and the governing equations that come out of these inclusions are provided and discussed. Each of the models are compared and contrasted to understand the limitations and advantages of each of them. This chapter also covers the changes necessary for each of the theories to be applicable to the varying support conditions that were analyzed.

Section 4 discusses the details of the methods employed for the vibrational mechanics study and the MEMS sensor calculations. The results of the study are presented and examined in detail, with final conclusions produced and listed. The final frequency calculations for the new MEMS device are also displayed in Section 4.

The final section of this report provides concluding remarks. Summarizing statements regarding each of the three main goals of this study are produced, and suggestions for further research that could stem from the work in this study are proposed.

2. REVIEW OF STRUCTURAL HEALTH MONITORING CONCEPTS AND PRACTICES

2.1 Introduction

The bridges and buildings that society uses and depends upon daily do not retain their strength and utility indefinitely. These structures deteriorate over time as they are continually exposed to harsh environmental conditions and continued or increasing loads. The issue of aging infrastructure has gained increasing interest over the last decade due to a few catastrophic failures as well as an expanding awareness of current infrastructure conditions. In August 2007, the Interstate 35W Bridge across the Mississippi River in Minneapolis, MN, suddenly collapsed, killing 13 people and injuring 144 [1]. This bridge was 40 years old and had been subjected to increased traffic and environmental loads over its lifetime, causing deterioration and ultimately the failure of some under-designed components. The I-35W Bridge is not an entirely unique case either. Much of the country's civil infrastructure is significantly aged and in need of attention. More than 35% of U.S. bridges were built more than 40 years ago [1], and according to the U.S. Department of Transportation (USDOT), in 2009, nearly a quarter of the country's bridges were either structurally deficient or structurally obsolete [2]. This growing problem needs to be addressed, and one of the ways engineers are doing so is through structural health monitoring. This is the process of tracking the condition of a structure over time to determine the nature and extent of damage that may exist and how this affects the integrity of the structure. Knowing this information can greatly improve the maintenance process and possibly prevent future damage or even collapse of civil infrastructure.

The field of structural health monitoring has grown significantly in recent years. There has been substantial research on the subject and there are continually more projects beginning in this field. The primary goal of structural health monitoring is to identify damage in a structure. Within damage identification, four different levels exist. The first level determines that damage is present within the structure. The second level includes locating the damage, while the third level assesses the extent of this damage. The final level uses the information from the first three steps to predict the remaining service life of the structure [3]. The following review will focus on methods that deal with the first three steps. There are two main method categories that exist in structural health monitoring to address these levels of damage identification. First, there are methods used for global monitoring. These methods result in information about the structure as a whole and how it responds to loads. The second category is local health monitoring methods. These methods are used to monitor local behavior at critical points on the structure. With local methods, the areas where damage is most likely must be known ahead of time for the analysis to be relevant. Depending on the information an engineer is interested in about a structure, and under which of these two categories that falls, there are multiple systems and types of sensors that can be employed to collect the desired information. This section will review the basic concepts behind both categories of structural health monitoring and the systems that have been considered or utilized to perform the analysis.

2.2 Global Health Monitoring Methods

The basic concept in global health monitoring methods is that the existence of damage will change the stiffness, mass, or damping properties of a structure and thus alter the global dynamic properties. The major benefit of this type of method is that the location of possible damage does not need to be known before installing a system, which is often not possible for complex structures. Methods of global health monitoring can be based on a number of different modal properties of a structure. The benefits and challenges to techniques based on each of these are discussed below. Also discussed are some methods based on acoustic properties of materials rather than modal properties of the structure.

2.2.1 Resonant Frequencies

Modal frequencies are one of the most basic vibrational properties of a structure. Every structure possesses unique resonant frequencies for each mode of vibration that are related to its mass and stiffness. This basic property can be used to detect the occurrence of damage by noting shifts in resonant frequency values. Although this is a very appealing concept, there are quite a few limitations that restrict the practical application of this method.

Resonant frequencies are a global parameter and do not provide any spatial information about a structure. It is evident that methods based on frequency shifts could only be effective at detecting the existence of defects and would require the use of an additional analysis technique to locate and assess the severity of any damage that may occur. Also, the sensitivity of frequency to damage is relatively low, especially for large structures. Significant damage must occur in the structure to cause a detectable change in resonant frequency for most measurement systems. A very precise monitoring system could possibly detect shifts from minor damage, but it then becomes difficult to separate shifts due to damage from changes caused by environmental and operational factors. Significant efforts were put forth to develop a damage detection method based on frequency shifts for offshore oil platforms during the 1970s and 1980s, but these were abandoned after encountering issues with machine noise, temperature variations, and changing mass due to varying fluid levels and marine growth [4]. It was impossible to separate changes caused by damage from all these other factors. Resonant frequencies at higher modes where the modes are associated with local responses become more sensitive to minor damage, but it is often unrealistic to excite and determine these modes. The one benefit of frequency-based methods over other global methods is that resonant frequencies could be found with less uncertainty than other modal parameters [5].

Many frequency-based health monitoring methods assume that cracking is the only form of damage that will occur. This significantly limits application possibilities. In concrete structures, for example, most of the stiffness is provided by the concrete and thus damage or deterioration of the reinforcing steel would not have a significant effect on the natural frequencies of the structure [6]. Using a frequency-based method may be able to detect cracks in the concrete but would miss reinforcement and confinement damage issues. Similarly, in steel structures, even a significant amount of corrosion may not have a detectable effect on the stiffness and would not cause a noticeable change in frequency. Therefore, frequency-based health monitoring methods can be effective in detecting significant damage from cracking, but they are not comprehensive, and other methods are needed to adequately monitor the health of a structure.

2.2.2 Mode Shape Vectors

The mode shape vectors associated with each mode of vibration are another basic dynamic property of a structure. These are also related to the mass, stiffness, and damping of a system and are affected when damage changes any of these parameters. A major advantage of damage detection methods based on mode shape over those based on frequency is the ability to locate the damage that occurs. Mode shape vectors are a spatial property and can provide information about both the existence and location of damage. The difficulty with this method is that it requires a significant number of measurement locations to accurately determine the mode shape and any changes caused by damage. Similar to frequency-based methods, modal shape monitoring methods also suffer from low sensitivity issues. Most damage that occurs is a local phenomenon and cannot be easily detected by studying the lower frequency mode shapes that are typically observed in large structures. In fact, mode shape changes can be even more subtle than frequency changes in typical structural response [6]. Mode shapes of higher frequency modes would be more sensitive to minor local damage, but as discussed before, these modes are difficult to induce. Mode shape-based methods possess most of the same limitations as frequency-based methods. A significant amount of damage must occur to be detectable and many types of damage would not have a relevant effect on mode shapes.

Overall, mode shape methods have the added benefit of the ability to locate damage, but are still insufficient for minor levels of damage and deficiencies other than cracks.

2.2.3 Mode Shape Curvatures

An alternative to using mode shapes to detect damage is to instead consider the mode shape curvature. The curvature is found by differentiating the mode shape vector twice. The value of curvature at a point in structure is equal to *M/EI*, so if the stiffness at a point is reduced by damage, the curvature at that point will increase. This can be used to both detect and locate damage in a structure, as well as possibly estimating the extent of damage by studying the amount of fluctuation in curvature values [7]. Studying the curvature is an improvement over using mode shapes because the curvature is far more sensitive to small changes in the structure than the mode shape. Thus, minor levels of damage may be able to be detected even in lower frequency modes with curvature-based methods. Another advantage is that there exists a direct relationship between mode shape curvature and bending strain for beams, plates, and shells. Bending strain has also been shown to be far more sensitive to low levels of damage than frequency and mode shape-based methods [4]. The greatest drawback of curvature methods is the accuracy. The techniques used for finding the second derivatives of the mode shapes can cause false readings of damage when none exist, which contaminates the results [8]. Also, it was found that the statistical uncertainty in finding curvature values was greater than in determining mode shape vectors or resonant frequencies [4]. Another difficulty with curvature-based monitoring methods can occur if there are not baseline data available for a structure. If damage is distributed throughout the structure before any data are collected, it may be challenging to detect damaged locations without knowing what the curvature values were before damage occurred [6]. Mode shape curvature methods are a more realistic option for large civil infrastructure health monitoring in that it only requires information from low frequency modes to be effective, but there are still accuracy and applicability issues that need to be resolved.

2.2.4 Dynamic Flexibility Matrix

Another method of global monitoring methods is based on differences in the dynamically measured flexibility matrix. The flexibility matrix is the inverse of the stiffness matrix for a structure and thus relates applied static force to structural displacement. The flexibility matrix is calculated from the mass normalized mode shapes and frequencies of a structure. Each column of this matrix represents the displacement pattern for a certain degree of freedom caused by a unit action applied to that degree of freedom. By studying the changes in the dynamic flexibility matrix over time, the existence and location of damage can be detected. The degree of freedom that displays the maximum variation in flexibility from the undamaged state represents the location of possible damage [7]. One of the main advantages of this method is that the flexibility matrix is inversely related to the modal frequencies, which makes it most sensitive to the lower-frequency modes that are more dominant in large structures [3].

There are some drawbacks to using a flexibility matrix method. In most applications only a few of the mode shapes will be calculated, which means that the flexibility matrix will only be approximate since its proper calculation requires all of the possible mode shapes. Also, this method works best when looking at flexibility changes between the completely undamaged state and the current condition. This requires either that measurements be taken immediately after construction of a structure or the use of a finite element model of the original structure. In many cases, researchers are interested in studying an already existing structure, so initial and undamaged measurements are impossible. Using a model of the original structure is a possible solution to this issue, but multiple assumptions usually need to be made to build the model which makes the analytical undamaged flexibility values approximate. Damage detection methods based on the dynamic flexibility matrix of a structure are an improvement over frequency and mode shape based

methods since they are more sensitive to lower frequencies, but may have accuracy issues due to the amount of approximation involved in the analysis.

2.2.5 Updating Modal Parameters

Another method to detect damage in structures involves updating modal property matrices such as mass, stiffness, or damping of a structural model to match the measured responses as closely as possible. These methods estimate the updated modal matrices through constrained optimization techniques based on equations of motion, the structural model, and the measured data [3]. These updated matrices are then compared to the original undamaged values to detect and locate damage. These methods are not as common as the previously discussed options because a number of problems exist with them. The original matrices for the undamaged case may be inaccurate to begin with and the optimization process does not produce a unique solution, so the updated matrices may not be representative of what is actually occurring in the structure. Also, the error minimization operation may cause the stiffness of undamaged elements to change which could lead to an abundance of false damage results [6]. Often the degrees of freedom from the analytical model matrices do not match the locations of measurement which can severely reduce the applicability or effectiveness of these methods [4]. Updating the modal properties of a structure is another option to detect damage that may have occurred, but there are significant obstacles to overcome with these methods.

2.2.6 Acoustic Properties

Another class of structural health monitoring methods is based on acoustic properties rather than modal properties. These methods are based on the measurement of waves propagating through the structural material. Some methods are based on how sound waves travel through different material anomalies, but these are mostly only employed in local health monitoring and will be discussed in the next section. Acoustic monitoring techniques, such as acoustic emission systems, can also measure how stress waves radiate through a structure. The basic concept behind acoustic emission methods is that stress waves are produced by a sudden release of energy due to micro-cracking occurring in the material. These stress waves can be picked up by acoustic emission sensors to detect cracking and even locate it through triangulation with multiple sensors [9]. A significant advantage to this type of global health monitoring is that it has the ability to detect damage events as they occur rather than after some analysis of the data. This can present a complication as well. This method is only applicable if data are being collected continuously, otherwise the stress emissions may be missed entirely. Continuous data collection may not be possible or cost effective in many cases. Some other drawbacks of this method are that the waves emitted by the micro-cracking can be very weak and difficult to detect over background noise and determining what type of damage has occurred is challenging [10]. Acoustic emission monitoring methods are a popular option because they can theoretically detect damage anywhere in a structure as it is happening. This could have significant applications in early warning systems that aim to shut down or evacuate structures if damage is indicating possible catastrophic failure.

2.3 Local Health Monitoring Methods

Once potential damage locations are determined from global monitoring methods, or if critical areas are initially known, local health monitoring methods are performed to assess the extent of damage and keep track of any damage progression. There are numerous techniques for performing local damage detection and assessment, but they all center on a few basic concepts. The properties measured and concepts employed in local health monitoring methods are discussed in this section.

2.3.1 Visual

Probably the most common type of local health monitoring practiced is visual inspection. This extremely simplistic method identifies damage in a structure simply by looking at it with the hope of recognizing changes and abnormalities. These methods are used very often, primarily due to the biannual bridge inspections mandated by the National Bridge Inspection Program enacted in 1967 [11]. This program requires current information on the nearly 600,000 bridges across the United States, and the adopted procedure for completing this requirement is visual inspection. These traditional techniques require immense amounts of time, closure of a bridge in many cases, and a great deal of manpower and other costs. Visual inspections also depend highly on the decisions and opinions of the inspector and can lead to large variations and subjectivity in the results. Furthermore, only outward appearance of a structure can be assessed, so even major internal damage could be missed for years [10]. Therefore, although this is still a popularly used method, it has multiple flaws, and more objective and comprehensive methods are needed to safely assess the current health of structures.

2.3.2 Strains or Displacements

Monitoring and assessing damage through either strains or displacements provide another favored option. As a structure is loaded and stressed, the material goes through strains and deflections in response, and if these strains or deflections exceed certain values, damage can be assumed. This type of method is typically used for predicted critical locations of a structure such as a connection or a potential weak spot that has been detected by a global detection method. Another monitoring application utilizing strain or displacement measurements is to watch an already known defect, such as a crack, to determine if the damage is worsening. Another parameter similar to displacement that may be monitored is the tilt or slope of a member. This is typically used to study pier behavior [10]. As environmental or loading conditions change, the angle of a bridge support may change, which could indicate weakness or failure. The primary problem with these methods is how localized their measurement capabilities are. Often strain is only measured over a few inches or less, and displacement and tilt are only recorded at one point on the structure. In general, though, monitoring methods based on strains or displacements are effective and commonly used.

2.3.3 Stresses or Loads

Another concept used in local health monitoring measures the stress or load that a part of the structure experiences. In relation to local health monitoring, if the stress or load occurring in a certain location is beyond a certain level, damage may be likely. Conversely, if the stress or load measurement decreases significantly or rapidly, it may be a signal that damage has occurred and the structure can no longer withstand the load it was previously supporting. These methods are utilized much less often because stresses or loads are substantially more difficult to directly measure than strain or displacement.

2.3.4 Acoustic Properties

Local health monitoring methods may also use acoustic properties to detect or measure damage. A few methods consider the propagation of sound waves through the material. The reflection of sound waves will change if anomalies such as air voids exist in the material. This principle is the basis for both chain dragging and tap tests. Chain dragging is used to determine bridge deck health and is a widely used and accepted local monitoring method. Tap tests are typically used to detect delamination between fiber reinforced polymer (FRP) sheets and concrete. Both of these methods possess subjectivity problems since the results depend on the inspector who is listening to the response. Two different inspectors can find entirely different conclusions. Another disadvantage with these two techniques comes from access concerns. With chain dragging, complete bridge closure is often required [10] and reaching testing locations for tap tests may be unsafe or impossible.

Another acoustic-based method employs the concept that stress wave propagation from a force is affected directly by mechanical properties [9]. This type of method, referred to as impact echo, involves applying a minor impact force to a structure and listening to its response. Based on the frequency of the wave response delaminations, voids, and cracks can be detected, as well as the depth at which they exist. This method has been found to be highly accurate, which is a significant advantage. A main disadvantage to this method is that many locations need to be tested in order to obtain a comprehensive understanding of the defects that may exist. Also, when applied to bridges, this technique requires that no traffic is present during testing, so lane closures are necessary [10].

2.4 Sensors Used in Structural Health Monitoring

All the health monitoring methods discussed require data values from the structure of interest to perform analysis and determine if any damage has occurred or if damage is probable. Although a few of the methods presented only require data from visual or manual inspection, these types of data are tedious and costly to obtain. Because of this issue, most research in the area of structural health monitoring has focused on the use of sensor systems to collect the necessary information for analysis. Two main types of quantities are typically measured with structural sensors: kinematic and environmental [12]. Environmental metrics such as temperature and humidity are commonly monitored to isolate the response of structure due to loading from these effects. Usually, the values of primary interest are of the kinematic type such as strain, displacement, and force. Therefore, the remainder of this section will focus on sensors that measure only kinematic quantities while realizing that these sensors would need to be combined with environmental data to properly analyze the state of a structure.

A multitude of different sensors have been developed and discussed for the use of structural health monitoring, the descriptions of which would at least fill an entire book. The following sections will present the most commonly used sensors that have been well established and tested, as well as some very promising recently developed sensor technologies, but this list is by no means a comprehensive presentation of available sensor technologies. Sensors that measure the dynamic vibrational properties required for global health monitoring will be presented first, then local kinematic sensors, and concluding with recent developments in the field of health monitoring sensors.

2.4.1 Accelerometers

Accelerometers measure the acceleration a particular location of a structure is experiencing due to either gravity or applied loads. Different versions of accelerometers have been used as measuring devices for many years because acceleration data can provide valuable information about the dynamic characteristics of a structure. Through post processing procedures, acceleration measurements can be used to calculate

frequency, damping, and mode shapes of a structure [11]. As discussed previously, these vibrational properties are useful in global health monitoring methods. Although accelerometers have long been employed for monitoring techniques, issues still exist with error development during the numerical integration of the data [13]. These devices also output a great deal of data, which can require intensive processing. Even with these challenges, accelerometers provide the best option for measuring dynamic properties of a structure. Four different types of accelerometers are commonly used and each have their own advantages and drawbacks, which will be discussed in the following paragraphs.

Piezoelectric Accelerometers

The most popular type of accelerometer of the four common options is the piezoelectric accelerometer. These sensors have many advantages, including small size, high output, durability, wide frequency range, and the ability to monitor a wide range of dynamic events [14, 11]. The basic components of a piezoelectric accelerometer are the base, a piezoelectric element, and a seismic mass. A basic setup for this type of sensor is shown in Figure 2.1. The piezoelectric elements in these sensors are the key components in the operation of the sensor. Piezoelectric materials have the unique property that they output an electrical signal proportional to the stress applied to the material [14]. As an acceleration is applied to the base of the sensor, the piezoelectric elements experience a force proportional to the mass they are connected to and thus to the acceleration being experienced. This force creates an electrical output that can be sent through a cable to a data acquisition system where it can be processed further. A significant advantage to these types of sensors is that they are self-generating. The piezoelectric material outputs an electrical signal without the need of a constant input electrical or power source [14]. When this type of accelerometer was originally invented, it required special low-noise cabling because the original signal from the piezoelectric material is susceptible to corruption from environmental effects and cable-generated noise [14]. Today, these accelerometers usually include electronics within the sensor that covert the signal so that it can be transmitted over long cable distances without any loss in quality [11]. The only downside to this addition is that it somewhat limits the temperature range in which the sensors can be used, but they still operate up to 350º F [14].

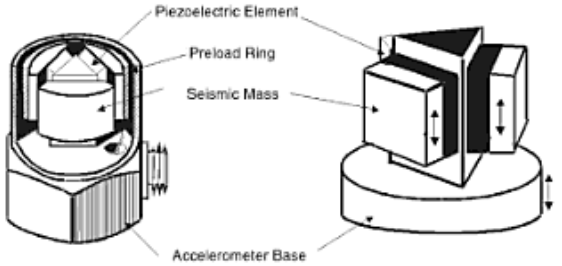

Figure 2.1 Basic Configuration of a Piezoelectric Accelerometer [14]

There are a few different options available with piezoelectric accelerometers. Two types of piezoelectric materials exist that can be utilized in these sensors: quartz or polycrystalline ceramics. Quartz is a natural material that is inherently piezoelectric and is therefore considered more stable than other material options and provides a better option for long-term accelerometers. Quartz is also immune to the pyroelectric effect, so the output is not affected by temperature change. One drawback to quartz is that it has low charge sensitivity, which limits its use in certain systems. Polycrystalline ceramics are man-made and forced to become piezoelectric through the process of poling. If these materials are exposed to drastic temperature changes or large electric fields, their properties can be significantly altered, which is their biggest disadvantage. Polycrystalline ceramics provide the benefit of being easily adapted to different properties, unlike quartz. The ceramics can be created to have high charge sensitivity or to withstand extremely high temperatures [14]. Both types of material have their usefulness, it simply depends on the application the

sensor will be used for. Three different structures of piezoelectric accelerometers are also available. The structure options are based upon the type of stress applied to the piezoelectric material in the sensor. The options are shear mode, flexural mode, and compression mode. Diagrams of each of these structure types are shown in Figure 2.2. The shear mode assembly allows for very small size, which is useful for high-frequency response. Flexural mode accelerometers are best for low-frequency and low-gravitational accelerations and are not sensitive to transverse motion. The last option, compression mode, is very rugged and can withstand high shock levels but can be more sensitive to thermal and strain effects since the piezoelectric material is in contact with the base [14].

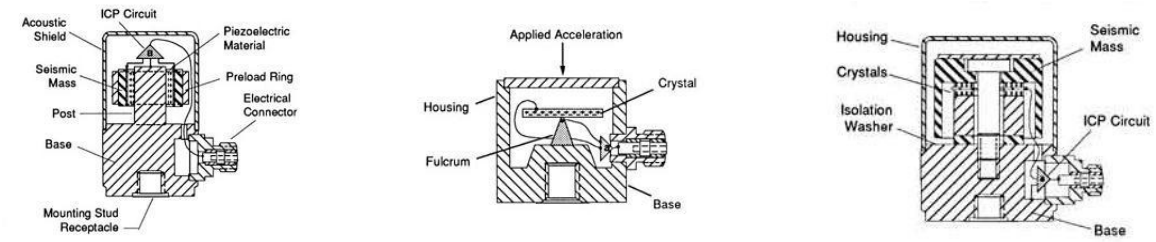

(a) Shear Mode (b) Flexural Mode (c) Compression Mode

Figure 2.2 Structure Types for Piezoelectric Accelerometers [15]

Piezoresistive Accelerometers

Another common accelerometer type utilizes piezoresistive strain gages. These strain gages use resistors made of single-crystal silicon. The electrical resistance of this material changes in proportion to the stress or force applied to it [11]. The common structure of piezoresistive accelerometers involves these strain gages attached to a cantilever bridge with a seismic mass attached. As the sensor experiences acceleration, the strain gages are stressed in flexure, which alters the electrical signal output by a Wheatstone bridge circuit. The main advantage to this type of accelerometer is that it can be produced in a very small size, which makes them useful in MEMS systems, which will be discussed in Section 2.4.7 [14]. Piezoresistive accelerometers also provide very low frequency response capabilities, which is another significant advantage. The main drawback to this sensor type is that it has a smaller dynamic range of measurement and requires a constant electrical input for the Wheatstone bridge circuit.

Capacitance Accelerometers

Capacitance accelerometers are very similar to piezoresistive accelerometers, since they measure an electrical change across a bridge, but these sensors measure a change in capacitance rather than resistance [14]. These accelerometers have very high resolution and can measure accelerations from the level of micro-g up to 100s of g, which is better than the resolution available from piezoresistive accelerometers [11]. Some disadvantages include a limited high-frequency range and a higher noise level than typical piezoelectric accelerometers.

Servo Force Balance Acclerometers

The last type of acclerometer that can commonly be found is the servo force balance type. The operation of these accelerometers differs greatly from the other three options discussed. All three previous sensor types measure the deflection of a seismic mass, which is proportional to acceleration, directly through different

electrical principles. Servo accelerometers instead keep the movement of an internal capacitor plate to a minimum by using electromagnetic forces to keep the mass in a neutral position. The required electromagnetic force necessary is proportional to the acceleration experienced [14]. The operation of this sensor occurs rapidly enough that there is virtually no relative movement between the plate and the supports, which reduces the effects of nonlinearities that can occur with the other three sensor types [11]. This type of accelerometer is far more accurate than the other three with measurement capabilities on the level of milli-g. The primary disadvantage to this option is the cost, which can be up to 10 times greater than other accelerometers. A figure of the basic principle behind servo force balance accelerometers is provided in Figure 2.3.

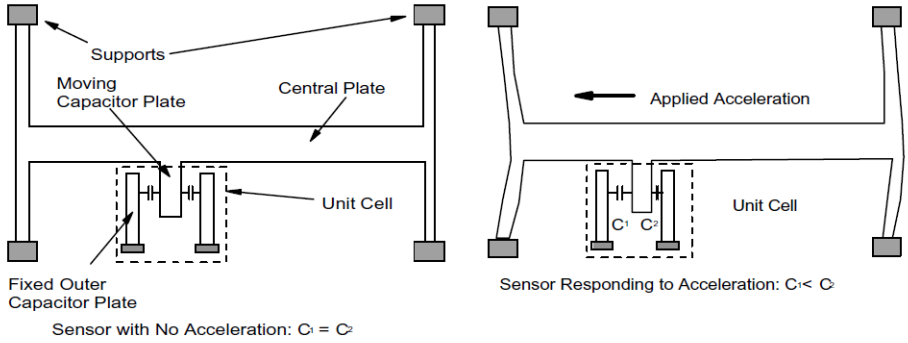

Figure 2.3 Diagram of Servo Force Balance Accelerometer Operation Principle [11]

2.4.2 Strain Gages

Strain gages are commonly used in the practice of structural health monitoring for a number of reasons. The greatest advantage of these sensors is that they are inexpensive and easy to install [16]. Although strain gages can only measure the strain of a structure at one location, the information gained from these sensors can be used in combination with a finite element model of the structure to help detect when damage may have occurred [17]. The use of strain gages in this type of method are based upon the principle that damage to a critical location will lead to a change in load path and thus a detectable difference in strain distribution [18]. The use of strain gages in structural health monitoring in this way is often because thorough research has been performed involving the interpretation of strain data, and this process is well understood [16]. Many varieties of strain gages exist, but two types are most commonly utilized in structural health monitoring methods and will be presented in the following paragraphs.

Electrical Resistance Strain Gages

Bonded foil resistance strain gages, also known as electrical resistance strain gages, are the most commonly used type of strain gage [11]. The principle behind these sensors is the fact that the electrical resistance of a conducting material is proportional to the length and inversely proportional to the cross-sectional area [19]. These strain gages consist of a metallic foil, usually arranged in a pattern to increase the length of the conductor, attached to a nonconducting film, which is then connected to the structure of interest with an epoxy. A diagram of this basic setup is shown in Figure 2.4. With this setup, the strain gage will deform with the member, and as the foil in the gage is stressed, the length and cross-sectional area will change, leading to a change in electrical resistance that can be measured [19]. The relationship between the change in electrical resistance and the change in length of the foil is known as the gage factor, which is unique to each sensor. With this factor, as well as basic constitutive laws, the relationship between strain and resistance can be determined. Because electrical resistance is also altered by changing temperatures, a

temperature control strain gage is commonly used, along with the gage attached to the structure, to isolate the strain due to kinematic loading.

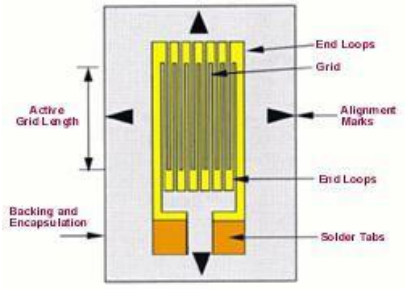

Figure 2.4 Basic Configuration of an Electrical Resistance Strain Gage [20]

Electrical resistance strain gages have a number of advantages and possible applications. These sensors can be employed on any structure material including steel, concrete, and composites. When applied to concrete members, the gage length tends to be longer to better average out the localized strain values due to discontinuities in the material, but this is a simple adjustment. Many other types of sensors, such as load cells, accelerometers, and more, also utilize electrical resistance strain gages within their setup, so these gages can be applied for more than just measuring local strain values [11]. Another advantage to electrical resistance strain gages is that they have been found to agree well with other types of strain gages in short-term monitoring situations [21, 22]. These sensors can also be used to determine principle strains when a strain gage rosette is employed [23]. Generally this type of strain gage is only used for short duration measurements, such as the strains caused by traffic loads, because they lose their accuracy over time due to their susceptibility to adverse effects from exposure to the elements. A few other issues exist with electrical strain gages besides their loss of accuracy over time. These sensors are ideally only sensitive to strain in the longitudinal direction of the gage, but they can be affected by transverse movement as well, which can reduce the accuracy [11]. They also require a constant power source to be operated and are more susceptible to noise effects than other types of strain gages. Even with these drawbacks, electrical resistance strain gages remain the most common option when using strain measurements in structural health monitoring.

Vibrating Wire Strain Gages

Vibrating wire strain gages are the other popular option for strain measurements. These sensors are known to provide excellent performance and long-term durability and can be installed externally on steel or concrete or embedded within a concrete member [11]. These sensors include a pretensioned steel wire that is fixed at both supports and an electromagnetic coil which is used to excite the wire and read its natural frequency. The wire is encased within a steel tube that can be applied to the desired member at each end. A diagram of the basic setup for this type of sensor is given in Figure 2.5 and a photograph of an external application option of this strain gage type is shown in Figure 2.6. This type of strain gage works by comparing the change in frequency of the pretensioned wire as the length of the wire changes to determine the strain experienced [24]. These strain gages have been shown to very stable over long periods of time, which makes them applicable for continuous measurement of slowly changing strains unlike electrical resistance strain gages [25]. The main disadvantages to this sensor option are that they are not applicable for measuring dynamic strains and there is the possibility for unequal strains to develop in the gage than in the member due to differences in thermal expansion [22]. Overall, these strain gages provide a reliable option for long-term strain measurements in structural health monitoring.

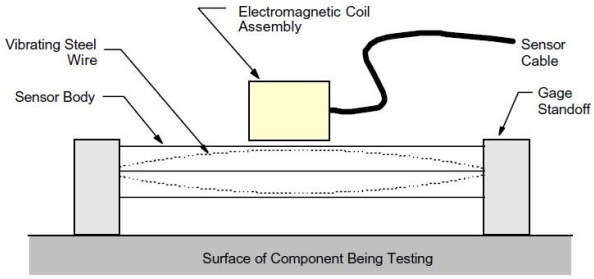

Figure 2.5 Schematic Diagram of the Operation of a Vibrating Wire Strain Gage [11]

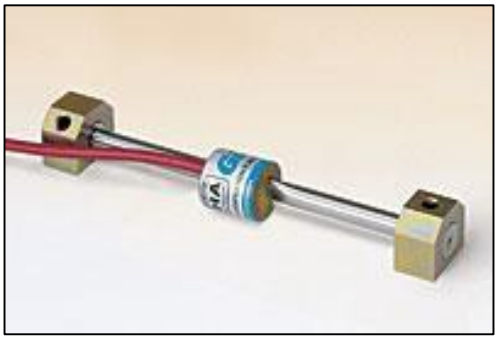

Figure 2.6 External Application Vibrating Wire Strain Gage Model [26]

2.4.3 Displacement Sensors

Displacement is another measurement parameter that is often of interest in the practice of structural health monitoring. Monitoring of displacements is commonly used to assess critical locations, such as across an expansion joint or over the length of a suspension cable in a bridge [10]. The two most common sensors utilized to measure displacement are linear potentiometers and linear variable differential transformers (LVDTs). The details of each of these are presented in the following paragraphs.

Linear Potentiometers

Linear potentiometers, also known as cable extension transducers, are composed of a spool with a length of stainless steel cable wound on it, a tension spring that keeps the spool loaded so that either direction of displacement can be measured, and a precision potentiometer. Usually, the main housing of the sensor is attached to a fixed location, with the end of the cable connected to the member or component whose displacement is being monitored. As the location of interest displaces, the cable extends from or retracts onto the spool, which rotates. The rotation of the spool moves the potentiometer. A potentiometer consists of a thin film resonator with a movable wiper, which is in contact with the electrical resistor. As the wiper moves across the resonator due to the rotation of the cable spool, a change in electrical resistance occurs, which is proportional to the displacement of the cable [11]. A diagram of the basic operation for an angular potentiometer is shown in Figure 2.7. The benefits of this type of displacement sensor include low cost, ability to measure large displacements, simplicity in operation, ease of installation, and higher accuracy and measurement range than LVDT sensors [11, 27]. Linear potentiometers also have some disadvantages in comparison with other displacement sensors in that they are not applicable for dynamic measurements or long- term continuous measurement due to temperature-related drift issues, and they are subject to wear problems over time because of the contact between the potentiometer wiper and resonator [11]. These displacement sensors still remain a positive option for accurate displacement measurements, especially if the expected displacements are large.

Linear Variable Differential Transformers (LVDTs)

Linear variable differential transformers (LVDTs) offer another common displacement sensor option. LVDT sensors are based upon the principle of mutual inductance. These devices consist of a hollow metallic cylinder containing a primary and two secondary electrical coils and a movable magnetic core. A diagram of this setup is provided in Figure 2.8. For the operation of this sensor, a voltage is applied to the

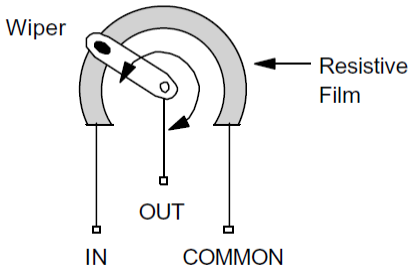

Figure 2.7 Schematic of Angular Potentiometer Operation [11]

primary central coil, which induces voltage in each of the secondary coils. These induced voltages are linearly related to the position of the magnetic core, which is attached to the member whose displacement is of interest [28]. As the magnetic core moves, the changing voltages in the secondary coils are converted to the amount of displacement [11]. LVDT sensors are generally more expensive than other displacement options, but they provide significant advantages. This type of sensor is capable of measuring dynamic displacements, can measure less than a nanometer of displacement, are suitable for use in very low temperatures with minimal loss in accuracy, and they also are virtually immune to wear damage because the moving magnetic core makes no physical contact with the electrical coils [11, 29, 28]. LVDT displacement sensors can be costly, but are applicable in many situations where linear potentiometers cannot be utilized.

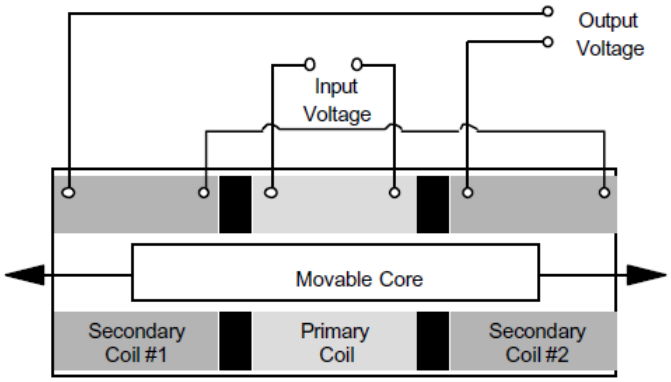

Figure 2.8 Linear Variable Differential Transformer Internal Composition Diagram [11]

2.4.4 Tiltmeters and Inclinometers

As mentioned previously, another metric that may be of interest in structural health monitoring is the slope or tilt of a particular location. Tiltmeters and inclinometers are the sensors utilized to measure this parameter. Three different options are available for tiltmeters, each with their own benefits. These will be compared in the following paragraphs.

Vibrating Wire Tiltmeters

Vibrating wire tiltmeters are composed of a pendulous mass, which is supported by a vibrating wire strain gage. As the sensor tilts, the gravitational force from the mass upon the strain gage will change due to this rotation. The frequency of the wire within the strain gage will shift because of this, and the relationship between this frequency and the angle of rotation can be determined. These sensors are designed for permanent measurements and are not applicable for dynamic slope changes, such as those due to traffic loads or an earthquake [11].

Electrolytic Tiltmeters

Electrolytic tiltmeters utilize a high-precision electrolytic tilt transducer and the primary sensing element. These devices are excited by an AC signal through the tilt transducer, and as the transducer tilts, internal electrodes are covered or uncovered by a conductive fluid within the device. As these electrodes are exposed or removed from the conductive fluid, the electrical resistance to the excitation signal is altered, which can be converted to a change in angle through a scaling factor. The primary benefit to this sensor type is that the angular movement of the sensor, and thus the member it is measuring, is compared to the gravity vector and therefore no external datum is necessary for operation. These sensors, again, are best for long-term angular changes rather than rapidly changing tilts [11].

Inertial-Based Inclinometers

Inertial based inclinometers are the main option for measuring dynamic tilt changes. The technology in these devices is similar to that of a servo force balance accelerometer. These inclinometers also contain a pendulous mass, and the motion of this mass is detected by an optical position sensor. The reading from this position sensor is compared with the original state, and a balancing current is produced and applied to a torque motor to return the mass to the original state. This basic operation is portrayed in a diagram in Figure 2.9. The balancing current required to keep the mass in the initial position is proportional to the tilt experienced by the sensor. These inclinometers are very accurate, with the ability to record changes in slope as minute as 0.1 seconds of a degree and are applicable where high levels of shock and vibration occur [11].

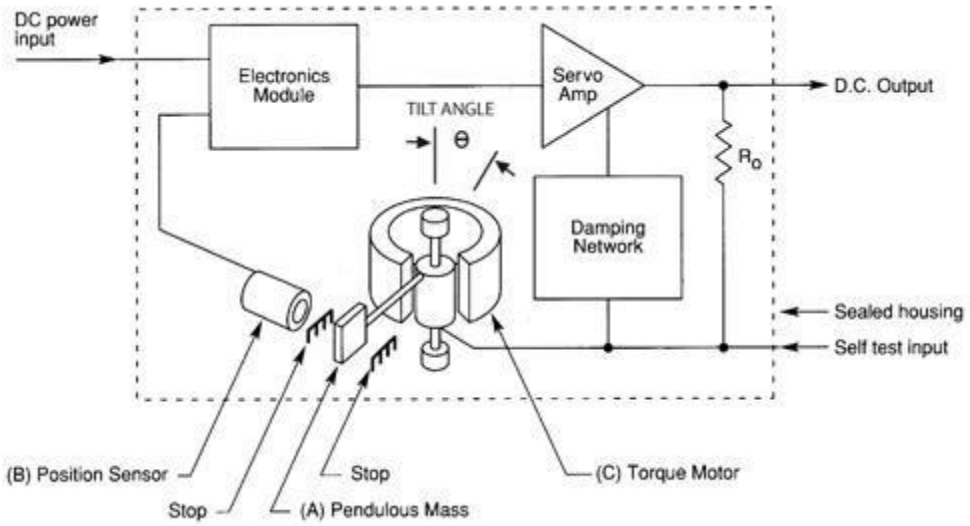

Figure 2.9 Diagram of the Operation of an Inertial Based Inclinometer [30]

2.4.5 Acoustic Emission Sensors

The most common type of acoustic emission sensor uses piezoelectric materials similar to the operation of a piezoelectric accelerometer. This type of sensor has been proven to be more durable and sensitive than other techniques based upon capacitance or laser-optics [31]. The piezoelectric material within the sensor experiences the force from the stress waves propagating from a crack and outputs a proportional electrical signal. A basic diagram of an acoustic emission sensor is shown in Figure 2.10. In order for these sensors to be applicable, they are typically used within a network of multiple sensors so that triangulation can be performed to determine the location of a stress wave source [11]. The best advantages of acoustic emission sensors is the ability to detect damage as it occurs and because the damage does not need to occur at the site of the sensor for it to be detected. Steel is the best material for the use of acoustic emission sensors because the stress waves do not attenuate as drastically and can be detected at farther distances [10].

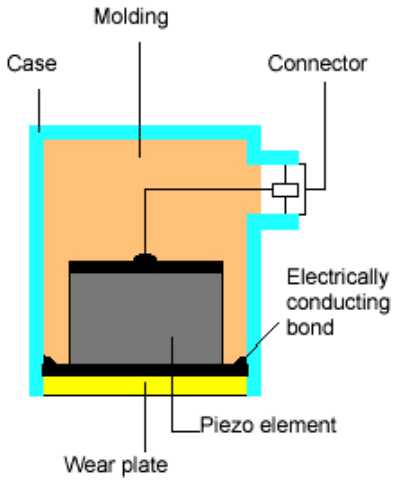

Figure 2.10 Diagram of an Acoustic Emission Sensor [31]

2.4.6 Fiber Optic Sensors

Fiber optic sensors are a relatively new technology that have a lot of promising applications. The basic operation of these sensors involves sending light beams down a fiber optic cable at regular intervals and measuring the changes that occur as this light is reflected [12]. Four different principles are commonly used to interpret these changes in light signals: interferometry, polarization, spectroscopy, and light intensity [32]. Interferometry-based fiber optic sensors monitor changes in the shape of light waves to measure environmental changes. When the principle of polarization is employed, the changes in optical polarization of a light signal are the measure of interest [33]. One of the most common types of fiber optic sensor types is a fiber Bragg grating (FBG) sensor, which is based on the principle of spectroscopy. Spectrally based sensors like FBG sensors monitor the change in wavelength of reflected light sources. Sensors using the principle of light intensity to measure how light intensity changes over the length of a fiber [10].

There are a large number of advantages to the use of fiber optic sensors, which has fueled the amount of research behind these devices. The most significant benefit to the use of fiber optics is the ability to measure multiple parameters with only one fiber because of the variety of principles that can be employed [11, 10, 12]. Another notable advantage over other types of sensors is the capability to measure changes along the entire length of a fiber rather than just at one particular location. Fiber optic sensors are also immune to electromagnetic interference, which is a common problem with many other sensor options.

Fiber optic technology can be easily incorporated into other devices such as accelerometers and electrical transducers and have been used to measure a variety of metrics, including strain, displacement, pressure, slope, acceleration, corrosion, loading, and cracking in concrete [32, 34]. Fiber optic strain gages that have been developed have shown the ability to detect strains with several orders of magnitude improvement over common electrical resistance strain gages and are immune to any transverse effects that often affects other strain gages [11, 12]. Two models of fiber optic strain gages are common: FBG sensors and extrinsic Fabry-Perot interferometric (EFPI) sensors. FBG sensors detect how the wavelength of reflected light changes due to applied loads. These sensors can be very small because the light changes are measured over a pattern written on the optical fiber which can be as short as needed. Fiber Bragg-based strain gages are less expensive than EFPI sensors but are not as accurate. In EFPI gages, the sensing element is not the optical fiber itself; instead, it consists of two mirrors placed such that the tips of optical fibers and the wavelength of reflected light between them is a function of the distance. EFPI strain gages are the most sensitive option but are also the most expensive [11]. The leading drawback to the use of fiber optic sensors comes from this higher cost, which has been a major obstacle in their process of becoming commonly utilized [11]. Further research and development are constantly being conducted in the field of fiber optic sensors for structural health monitoring to discover new applications and increase the affordability so that their distinct advantages may be more available in the future.

2.4.7 Microelectromechanical Systems (MEMS) Sensors

Sensors utilizing microelectromechanical systems (MEMS) are another recent technology development in the field of structural health monitoring. One of the significant advantages of MEMS sensors is the ability to both sense and actuate. This means that within the same device, data can be collected and partially processed before being transmitted. This is usually done by including an on-board microprocessor within the sensor system that can be used to convert the signal to digital, perform basic calculations, or provide interfacing functions, which can greatly reduce the amount of data processing required [12]. MEMS sensors also have the benefit of miniature size, so they are applicable in situations where typical sensors are too large. The common manufacturing process for MEMS devices also presents the possibility of large scale

productions with relatively low cost [35]. One application found in research is a MEMS-based transducer to be used for acoustic emission detection. This type of acoustic emission sensor could include multiple transducers, each with a narrow and highly sensitive resonant frequency, which together still cover the frequency range of interest. This could help the process of differentiating environmental noise from actual stress waves caused by acoustic emission events and greatly improve the accuracy overall [35]. MEMS-based strain sensors have also been developed using piezoresistive principles that could improve resolution and sensitivity as well as consume less energy than common strain gages [36].

MEMS sensors also have a great deal of potential for use outside of structural health monitoring. One of the promising applications is the use of MEMS sensors in microbiology. MEMS sensors have been shown to be ideal for measurement of force and displacement on the single-cell level with the ability to study a large population of cells at one time [37]. This ability has been utilized in tests to recognize and remove cervical cancer cells from a mixed cell population. The hope is for these sensors to be a diagnostic tool because they can process a large population rapidly with low cost [38]. A potential new MEMS-based sensor with possible applications in both structural health monitoring and microbiology is being developed; and preliminary calculations and investigations for this device are discussed in Section 4.

2.5 Summarizing Remarks

The field of structural health monitoring has grown significantly over the last few decades. The aging infrastructure in the United States and around the world, as well as rapidly improving technologies, have helped this growth. Multiple methods have been investigated and tested to assess the overall state of a structure through global health monitoring as well as concepts to determine if issues are present on a more local level. Numerous varieties of sensors and devices have also been developed to accurately gain the data required for global and local assessment practices, with some very successful and applicable options available. Even with all this progress, there still exists considerable issues and complications with many of the methods and technologies that have been developed. Although an increasing number of bridges and other structures are being studied through structural health monitoring concepts, much more research and development need to be performed before measurement and investigation through these methods can be feasible for all structures. The goal to continually improve the accuracy, applicability, and cost effectiveness of structural health monitoring is the impetus behind the development of the MEMS device investigated in Section 4 and many similar current projects and ideas for the future. Through all this continued research, the achievement of monitoring all bridges and structures may someday be met so that tragedies such as the I-35W bridge collapse will never occur again.

3. THEORY OF BEAM VIBRATION

3.1 Introduction

The vibrating beam is a well-studied mechanics problem with a multitude of practical applications in engineering. Problems involving a vibrating beam are typically approached using one of the common beam theories, which were all introduced by 1921 [39] and have been thoroughly studied. The three most typically used beam theories are the Euler-Bernoulli, Rayleigh, and Timoshenko theories. While for many engineering applications, the use of one of these theories provides reasonable results, all three of them still rely upon a few basic assumptions. These assumptions take fully three-dimensional elasticity theory and simplify it to an approximate one-dimensional theory. A main component missing from the collection of research on the vibrating beam is an investigation into when these assumptions begin to fall apart. In order to confidently utilize these beam theories, their limitations should be well understood. In this section, a fourth method to analyze vibrational beam mechanics is introduced that better approximates a fully three-dimensional elasticity theory. This approach will be employed to study the accuracy of the common beam theories and the point at which they fail to be acceptable analysis tools. When studying the effectiveness of common beam theories, three different boundary condition cases will be evaluated: fixed-free, fixed-fixed, and simply-supported. The following sections will discuss the concepts applied in each theory and the development of equations of motion and boundary conditions for each. Frequency equations for each of the proposed end condition cases will also be introduced and explained.

3.2 Basic Beam Theories in Mechanics

3.2.1 Euler-Bernoulli Beam Theory

The Euler-Bernoulli beam theory (also known as the classical beam theory, Euler beam theory, Bernoulli beam theory, or Bernoulli-Euler beam theory), is the most commonly used theory. The early development of this theory can be traced back to the early 18th century. Two different Bernoulli's contributed to this model, but it began with Jacob Bernoulli (1654-1705). Jacob was the first to use infinitesimal calculus to study the deflection curve of an elastic bar. He developed an equation that described a proportional relationship between the bending moment at a certain point in a beam and the curvature at that location [40]. Although the constants he found in this equation were later found to be incorrect, the basic principle was true and later used by Euler. Leonard Euler (1707-1783) made significant advancements to mathematics and mechanics of materials, and he happened to be the pupil of another Bernoulli, Jacob's nephew, Daniel. Daniel Bernoulli (1700-1782) contributed to this theory in two ways. He was the first to derive the differential equation that governs the lateral vibrations of a prismatic bar. He also made a crucial suggestion that Euler use variational calculus in deriving equations for the deflection curves of elastic beams. Euler took this suggestion, and also adopted Jacob Bernoulli's principle, when he expanded the study of beam mechanics. Euler showed how differential equations of motion could be derived and how the motion of a particle could be found by integrating these equations. He used these principles to establish formulae for the frequencies and mode shapes of beams with varying end conditions [40]. The final equations and principles described in Euler's work contrive the final form of the Euler-Bernoulli beam model.

This beam model is the most commonly used theory because it is very simple and provides acceptable results for many engineering problems. This theory includes both the strain energy from bending and the kinetic energy from transverse displacement but does not consider the effects of rotary inertia or shear

displacement. Due to ignoring these two contributions, this model tends to overestimate the natural frequencies of a vibrating beam, especially for higher modes of vibration [39]. The Euler-Bernoulli model also lacks accuracy as the beam becomes less slender. When analyzing low modes of vibration for slender beams, the contributions from rotary inertia and the effect of shear are negligible, but this does not describe many engineering problems. Therefore, more advanced beam models have been developed to improve the results for less slender beams and higher modes of vibration.

3.2.2 Rayleigh Beam Theory

It was almost a century after the work of Euler before a new contribution was made to beam mechanics theories. This improvement came from Lord Rayleigh (1842-1919) in his treatise "The Theory of Sound" in 1877. In this work, Rayleigh proposed a method of finding frequencies of vibration directly from an energy view by assuming a suitable form for the type of motion, rather than solving differential equations. He then used this approximate method to study transverse vibrations of beams. His most important contribution from this study was a correction that allowed for rotary inertia that had been previously ignored [40]. When the equations of motion that include this effect of the rotation of the cross section are employed, it is called the Rayleigh beam theory. The addition of this factor provides a slight improvement over the Euler-Bernoulli model by slightly reducing the overestimation of the natural frequencies. The Rayleigh model still does not incorporate the contribution of shear displacement, and thus does not entirely fix the high frequency results [39].

3.2.3 Timoshenko Beam Theory

In 1921, Stephen Timoshenko (1878-1972) proposed a beam theory that presents significant advancements over the Rayleigh beam theory. The Timoshenko beam theory, sometimes known as the first order shear deformation theory, expands upon the Euler-Bernoulli theory by incorporating the effects of both rotary inertia and shear deformation. In his calculations, Timoshenko found that the change due to the addition of shear was four times greater than the change from the inclusion of rotary inertia [41]. Because of this, the Timoshenko beam theory is more popular than the Rayleigh model. This model results in far more accurate frequency values for non-slender beams and high frequency modes than either of the other two options. In these two situations, the effect of shear forces on beam deflections is significant and cannot be neglected [39]. Therefore, the use of the Timoshenko model has significant applications beyond the potential use of either the Euler-Bernoulli or Rayleigh beam theories. An essential component in the Timoshenko model is the shape factor. This parameter is utilized to account for the variation of shear stress across the cross section. The shape factor is a function of the shape of the cross-section, Poisson's ratio, and the frequency of vibration [39]. Usually, the dependence on the frequency is ignored, leading to less accurate results. In general, the Timoshenko model provides a substantial improvement over both the Euler-Bernoulli and Rayleigh beam theories and is still widely used.

3.2.4 Elasticity-Based Beam Theory

In order to study the accuracy of typical beam theories, a fully three-dimensional elasticity approach is proposed. A more advanced theory is considered because all three of the discussed theories still rely on a number of basic assumptions [39]. These include:

- The axial dimension is significantly larger than the other two.
- The Poisson effect is neglected.
- Planes perpendicular to the neutral axis remain perpendicular after deformation.

- The material is isotropic.
- The material is linear elastic.
- The cross-section is symmetric.
- The angle of rotation is small enough that the small angle approximation can be used.

The proposed elasticity theory will remove a few of the assumptions listed above. The problem of the transversely vibrating beam typically cannot be solved exactly, so solutions using Ritz-based approximations are utilized in this advanced method. This allows for the inclusion of the Poisson effect and the ability to calculate accurate frequencies for non-slender beams and even anisotropic materials. The details of this fully three-dimensional elasticity method are described in the following section.

3.3 Governing Beam Theory Equations

Based on the assumptions made and the different mechanical effects that are included, each beam model has unique governing equations associated with it. These equations represent the principles included in each model and the motion of the beam under loading or vibrations. A few different categories of equations are presented and explained for each model in this section.

A key tool employed in the analysis of beam response is the assumption of a displacement field based on certain kinematic restraints imposed by the model. The general purpose of restraining the motion of a particle through a displacement field representation is to minimize the number of dimensions in a problem. By limiting the dimensions considered in analysis, the computation can be significantly simplified. As the theories progress from the simplest representation, Euler-Bernoulli Theory, to the most complex, Elasticity Theory, the constraints on the motion are reduced leading to more complex displacement fields. The assumed displacement field for each model discussed in this chapter will be introduced in the following paragraphs.

Another common method to characterize the response of beam uses the governing differential equation or equations of motion for a particular model. This is generally developed using Hamilton's principle [39]. This principle is based upon the Lagrangian function, sometimes called L, which is given as

$$L \equiv U - K + A. \tag{3.1}$$

In this function, U represents the total strain energy of the beam, K is the total kinetic energy of the beam, and A represents the potential energy of the loading [42]. For the study discussed in this paper, only free vibration is considered and the loading term A drops out. The equation for Hamilton's principle can be expressed as

$$\delta \int_{t_0}^{t_1} L dt = 0. \tag{3.2}$$

This principle states that:

> *The time integral of the Lagrangian function over a time interval t_0 to t_1 is an extremum for the "actual" motion with respect to all admissible virtual displacements which vanish, first, at instants of time t_0 and t_1 at all points of the body, and, second over S_u, where the displacements are prescribed, throughout the entire time interval [42].*

The Lagrangian function can be found for each of the beam theories discussed based upon the assumed displacement field and the different displacement effects that are included. By employing this principle, the governing differential equation of motion can be found for each theory. Along with the equation of motion, the boundary conditions that must be satisfied are also developed using this principle. Using the developed equations of motion, formulas for the spatial solution to each problem have been found. The differential equations of motion, boundary conditions, and spatial solutions that have been developed for the three typical beam theories will be discussed in this section. For the full elasticity theory, a generalized eigenvalue problem is developed rather than a differential equation to represent the motion of a beam, which will also be presented in this section.

The same variables will be used for the discussion of all four models. In accordance with common practice for beam theory discussion, dimensionless variables will be employed for the geometric and vibrational parameters. The notation used follows

- $x_1 = x$ = the dimension parallel to the width of the beam
- $x_2 = y$ = the vertical or transverse dimension
- $x_3 = z$ = the axial dimension
- $u_1 = u$ = the unknown displacement in the x-direction
- $u_2 = v$ = the unknown vertical or transverse displacement
- $u_3 = w$ = the unknown axial displacement
- L^* = beam length
- A^* = cross section area
- $\boldsymbol{I}^*$ = moment of inertia
- ρ^* = material density
- E = Youngs Modulus
- G = Shear Modulus
- ω_i^* = angular frequency
- $L = L^*/\boldsymbol{L}^*$ = dimensionless beam length
- $A = A^*/\boldsymbol{L}^{*2}$ = dimensionless area

- $I = I^*/L^{*4}$ = dimensionless moment of inertia
- $\rho = \rho^* L^{*6}\omega_1^{*2}/(EI^*)$ = dimensionless density
- $\omega_i = \omega_i^*/\omega_1^*$ = dimensionless angular frequency

3.3.1 Euler Bernoulli Model

Displacement Field

The Euler-Bernoulli beam theory contains only one unknown variable, the transverse displacement of the beam centroid. This displacement is only a function of the axial dimension, which is the reason this is considered a one-dimensional theory. Since the Poisson effect is neglected in this model, the assumed displacement field is of the form

$$u(x, y, z) = 0$$

$$v(x, y, z) = v(z)$$

$$w(x, y, z) = -y\frac{dv}{dz}$$

Equation of Motion and Boundary Conditions

The Lagrangian function determined from the kinetic and potential energy terms included in the Euler-Bernoulli model is given by [39]

$$L = \frac{1}{2}\int_0^1 \left[\rho A\left(\frac{\partial v(z,t)}{\partial t}\right)^2 - \left(\frac{\partial^2 v(z,t)}{\partial z^2}\right)^2\right] dz. \tag{3.3}$$

When this function is substituted into Hamilton's principle, the equation of motion and boundary conditions are determined. This governing differential equation of motion is given by [39]

$$\rho A\frac{\partial^2 v(z,t)}{\partial t^2} + \frac{\partial^4 v(z,t)}{\partial z^4} = f(z,t). \tag{3.4}$$

As mentioned before, only free vibration is considered for the vibrational study in this paper, so the forcing function, $f(z, t)$, is set to zero. The boundary conditions, which need to be satisfied for this equation to be applicable, are [39]

$$\frac{\partial^2 v}{\partial z^2}\delta\left(\frac{\partial v}{\partial z}\right)\Bigg|_0^1 = 0 \qquad \frac{\partial^3 v}{\partial z^3}\delta v\Bigg|_0^1 = \tag{3.5}$$

Each of the terms in these boundary conditions have a physical meaning that they represent. The expression v represents the transverse displacement, and thus, the first derivative $\partial v/\partial z$ represents the slope. The second

derivative of the displacement $\partial^2 v/\partial z^2$ represents the moment, and finally the third derivative $\partial^3 v/\partial z^3$ is the shear force. The δ operator signifies the variation of the term it is operating on. Therefore, if $\delta v = 0$ it means that the displacement is constant, or known. It does not necessarily mean that the value of the displacement is zero. Similarly, the expression $\delta(\partial v/\partial z) = 0$ indicates that the slope is known [39].

There are four different possible support conditions that can be considered for a beam. These are: a free end where the displacement and slope are unknown, a fixed end where the moment and shear are unknown, a hinged end where the shear and slope are unknown, and a rolling end where the displacement and moment are unknown. Each of these four possibilities have their own respective boundary condition combinations that must be satisfied. These are listed below.

- for a free end: $\frac{\partial^2 v}{\partial z^2} = 0$ and $\frac{\partial^3 v}{\partial z^3} = 0$
- for a fixed end: $v = 0$ and $\frac{\partial v}{\partial z} = 0$
- for a hinged end: $v = 0$ and $\frac{\partial^2 v}{\partial z^2} = 0$
- for a rolling end: $\frac{\partial v}{\partial z} = 0$ and $\frac{\partial^3 v}{\partial z^3} = 0$

These known boundary conditions will be utilized to find mode shape and frequency equations for the varying beam cases that will be studied.

Spatial Solution

To simplify the analysis of different beam conditions, the principle of separation of variables has been used to isolate an equation for transverse displacement that is dependent on the axial direction only, and not time [39]. This new equation is referred to as the spatial solution and it is of the form

$$V(z) = C_1 \sin az + C_2 \cos az + C_3 \sinh az + C_4 \cosh az. \tag{3.6}$$

In this equation, the parameter a is the dimensionless wave number. This value represents $1/2\pi$ times the number of wave cycles in a beam length [39]. For the Euler-Bernoulli model, this number is given by

$$a = \rho A \omega^2. \tag{3.7}$$

Since the spatial solution equation listed above is not dependent upon time, the boundary condition equations need to be altered before their substitution into the spatial solution. The terms in the spatial boundary conditions become ordinary derivative, rather than partial and the variable $v(z, t)$ is replaced with $V(z)$. These updated boundary conditions can be substituted into the spatial solution, resulting in a system of equations. This system of equations can be solved to find the unknown C factors and equations for the vibrational frequency of different beam cases. These will be presented in a later section.

3.3.2 Rayleigh Beam Theory

Displacement Field

The assumed displacement field for the Rayleigh beam model is identical to the Euler-Bernoulli model. The inclusion of rotational inertia effects alters the kinetic energy of the beam, but does not affect the assumed displacement relationships. The model still only has the one unknown variable of the transverse displacement and ignores the Poisson effect. Therefore the displacement field is still of the form

$$u(x, y, z) = 0$$

$$v(x, y, z) = v(z)$$

$$w(x, y, z) = -y\frac{dv}{dz}$$

Equations of Motion and Boundary Conditions

The Lagrangian function for the Rayleigh beam theory includes the term for the kinetic energy due to the rotation of the cross section [39]. With this additional term the Lagrangian becomes

$$L = \frac{1}{2}\int_0^1 \left[\rho A\left(\frac{\partial v(z,t)}{\partial t}\right)^2 + \rho I\left(\frac{\partial^2 v(z,t)}{\partial t \partial z}\right)^2 - \left(\frac{\partial^2 v(z,t)}{\partial z^2}\right)^2\right] dz. \tag{3.8}$$

The addition of this kinetic energy term from the rotation alters the governing differential equation of motion found using Hamilton's principle for the Rayleigh beam model. With this factor included the form the of equation becomes [39]

$$\rho A\frac{\partial^2 v(z,t)}{\partial t^2} + \frac{\partial^4 v(z,t)}{\partial z^4} - \rho I\frac{\partial^4 v(z,t)}{\partial z^2 \partial t^2} = f(z,t). \tag{3.9}$$

Similar to the Euler-Bernoulli model, the function $f(z, t)$ is set to zero to represent free vibration. The boundary conditions that need to be satisfied for this model are [39]

$$\left.\frac{\partial^2 v}{\partial z^2}\delta\left(\frac{\partial v}{\partial z}\right)\right|_0^1 = 0 \qquad \left.\left(\frac{\partial^3 v}{\partial z^3} - \rho I\frac{\partial^3 v}{\partial z \partial t^2}\right)\delta v\right|_0^1 = 0. \tag{3.10}$$

The boundary condition terms that represent the displacement, slope, and moment are the same as in the Euler-Bernoulli model. The term that represents the shear force has changed to become ($\partial^3 v/\partial z^3 - \rho I\, \partial^3 v/\partial z \partial t^2$)). Since this boundary term now includes a time derivative, it will have to be redefined to be applicable with the spatial solution. This is discussed in the following paragraph. Again, there are four possible support conditions, each with unique boundary condition combinations. These are listed below.

- for a free end: $\frac{\partial^2 v}{\partial z^2} = 0$ and $\left(\frac{\partial^3 v}{\partial z^3} - \rho I \frac{\partial^3 v}{\partial z \partial t^2}\right) = 0$
- for a fixed end: $v = 0$ and $\frac{\partial v}{\partial z} = 0$
- for a hinged end: $v = 0$ and $\frac{\partial^2 v}{\partial z^2} = 0$
- for a rolling end: $\frac{\partial v}{\partial z} = 0$ and $\left(\frac{\partial^3 v}{\partial z^3} - \rho I \frac{\partial^3 v}{\partial z \partial t^2}\right) = 0$

Spatial Solution

By separating the time and spatial variables in the governing equation of motion, the spatial solution for the Rayleigh beam theory was found to be [39]

$$V(z) = C_1 \sin az + C_2 \cos az + C_3 \sinh bz + C_4 \cosh bz. \tag{3.11}$$

In this model there are two dimensionless wave numbers, which are defined by the following expressions [39].

$$a = \sqrt{\frac{\rho I \omega^2}{2} + \sqrt{\left(\frac{\rho I \omega^2}{2}\right)^2 + \rho A \omega^2}} \tag{3.12}$$

$$b = \sqrt{-\frac{\rho I \omega^2}{2} + \sqrt{\left(\frac{\rho I \omega^2}{2}\right)^2 + \rho A \omega^2}} \tag{3.13}$$

The boundary conditions listed in the previous section need to be updated to be compatible with the spatial solution. For the displacement, slope, and moment conditions, the partial derivatives become ordinary derivatives and the $v(z, t)$ variable is changed to $V(z)$ similar to in the Euler-Bernoulli model. The shear term in this case cannot be updated as simply as before though, since it includes a spatial derivative. In this case, the expression for shear in the boundary terms becomes [39]

$$\frac{d^3V}{dz^3} + \rho I \omega^2 \frac{dV}{dz}.$$

These spatial boundary conditions can be applied to the spatial solution to determine the unknown C constants and frequency equations for the Rayleigh model. These solutions will be discussed in a following section.

3.3.3 Timoshenko Beam Theory

Displacement Field

Since the Timoshenko beam theory includes deformation due to shear, the total angle of rotation for a cross section is now the sum of both the bending and shear deflection effects. Thus, the Timoshenko model increases the number of unknown variables to two. The total cross sectional rotation due to shear is now unknown as well as the transverse displacement. In the spatial description, the variable for total rotation is $\Psi(z)$. This variable is only dependent upon the axial dimension, similar to the transverse displacement. The Timoshenko beam theory is therefore still only a one-dimensional theory. Since it is one-dimensional, the Poisson effect is again neglected and the assumed displacement field becomes

$$u(x, y, z) = 0$$

$$v(x, y, z) = v(z)$$

$$w(x, y, z) = -y\Psi(z).$$

Equations of Motion and Boundary Conditions

If strain-displacement and constitutive laws are used with the above displacement field to determine the values for stress, a significant problem is encountered. Finding stress through this method results in a constant shear stress throughout the cross section. This is physically impossible since the outside surfaces of the beam are traction-free. Timoshenko realized this issue and introduced the shear factor, which was discussed before. This factor partially corrects this issue, but is still somewhat approximate. For the purposes of the vibrational study in this paper, a shear factor that is dependent on the cross section shape and Poisson ratio will be used for calculations involving an isotropic material. For a rectangular cross-section, the shape factor is given as [39]

$$k^k = \frac{10(1 + v)}{12 + 11v}. \tag{3.14}$$

For an orthotropic material, determining an adequate shear factor is not so simple. Instead of the equation listed above, a new shear correction factor was determined using Hutchinson's beam theory by Puchegger and co-workers [43]. The shear factor found through this method is related to the cross section shape, two Poisson ratios, two shear moduli, and Young's modulus in the axial direction.

The derived equation is given by

$$k^k = -\frac{E_z}{G_{zy}[(A/I_x^2)C_4 + \nu_{zy} - (I_y/I_x)\nu_{zx}]}. \tag{3.15}$$

In this equation C_4 is a constant that can be found using the following formula.

$$C_4 = \int_A [-y^2\nu_{zy}f_1(x,y) + x^2\nu_{xz}f_1(x,y) - 2yx\nu_{xz}f_2(x,y) - E_z\left(\frac{f_1(x,y)^2}{G_{zy}} + \frac{f_2(x,y)^2}{G_{xz}}\right)]dxdy \tag{3.16}$$

The functions f_1 and f_2 can be found in the paper by Puchegger and others [43].

By using these shear factors, the potential energy from shear can be included in the Timoshenko beam model. The Lagrangian function is therefore given by [39]

$$L = \frac{1}{2}\int_0^1 \left[\rho A\left(\frac{\partial v(z,t)}{\partial t}\right)^2 + \rho I\left(\frac{\partial^2 v(z,t)}{\partial t \partial z}\right)^2 - \left(\frac{\partial \alpha(z,t)}{\partial z}\right)^2 - k'GA\left(\frac{\partial v(z,t)}{\partial z} - \alpha(z,t)\right)^2\right] dz. \tag{3.17}$$

Since there are two unknown variables for this theory, using Hamilton's principle produces two differential equations of motion, which are [39]

$$\begin{aligned} \rho A\frac{\partial^2 v(z,t)}{\partial t^2} - k^k GA\left(\frac{\partial^2 v(z,t)}{\partial z^2} - \frac{\partial \alpha(z,t)}{\partial z}\right) &= f(z,t) \\ \rho I\frac{\partial^2 \alpha(z,t)}{\partial t^2} - \frac{\partial^2 \alpha(z,t)}{\partial z^2} - k^k GA\left(\frac{\partial v(z,t)}{\partial z} - \alpha(z,t)\right) &= 0. \end{aligned} \tag{3.18}$$

The function $f(z, t)$ is set to zero again because only free vibration is considered for the analysis. The boundary conditions that need to be satisfied for these equations are given by

$$\frac{\partial \alpha}{\partial z}\delta\alpha\Big|_0^1 = 0 \qquad\qquad k'GA\left(\frac{\partial v}{\partial z} - \alpha\right)\delta v\Big|_0^1 = 0, \tag{3.19}$$

where $\alpha(z, t)$ represents the total rotation of the cross section [39].

The boundary condition terms have a different appearance in the Timoshenko model because of the additional variable of section rotation, but the physical meaning of the terms is very similar to that of the Euler-Bernoulli and Rayleigh beam theories. The expression for the transverse displacement is still v, but the term for the slope is now simply represented by α rather than the derivative of the displacement. Similarly, the moment term is now $\partial\alpha/\partial z$ rather than the second derivative of transverse displacement. The shear term in this model is quite different from the previous two theories since the shear factor and shear modulus are now included. The expression for shear is now $k^kGA(\partial v/\partial z - \alpha)$. With these new boundary condition expressions, the combinations for each of the four possible support conditions have changed and are listed below.

- for a free end: $\frac{\partial \alpha}{\partial z} = 0$ and $k'GA\left(\frac{\partial v}{\partial z} - \alpha\right) = 0$
- for a fixed end: $v = 0$ and $\alpha = 0$
- for a hinged end: $v = 0$ and $\frac{\partial \alpha}{\partial z} = 0$
- for a rolling end: $\alpha = 0$ and $k'GA\left(\frac{\partial v}{\partial z} - \alpha\right) = 0$

Spatial Solution

In order to determine spatial solutions for both the transverse displacement and the total rotation, the governing equations provided in the previous section must first be decoupled so each equation only contains one of the unknown variables [39]. The decoupled form of these equations is given below.

$$\begin{aligned}
&\frac{\partial^4 v}{\partial z^4} - \left(\rho I + \frac{\rho}{k'G}\right)\frac{\partial^4 v}{\partial z^2 \partial t^2} + \rho A\frac{\partial^2 v}{\partial t^2} + \frac{\rho^2 I}{k'G}\frac{\partial^4 v}{\partial t^4} = 0 \\
&\frac{\partial^4 \alpha}{\partial z^4} - \left(\rho I + \frac{\rho}{k'G}\right)\frac{\partial^4 \alpha}{\partial z^2 \partial t^2} + \rho A\frac{\partial^2 \alpha}{\partial t^2} + \frac{\rho^2 I}{k'G}\frac{\partial^4 \alpha}{\partial t^4} = 0
\end{aligned} \tag{3.20}$$

For these equations, when the method of separation of variables is applied, it is found that two different cases need to be considered for the spatial solutions [39]. These two cases are when the frequency is less than a critical value, or if it is above this value. In Han and co-workers work, it was shown that this critical frequency value is equal to $\sqrt{k^1 GA/pI}$ and is referred to as w_c.

For the case when $\omega < \omega_C$ the form of the spatial solutions for the transverse displacement and total section rotation are given by

$$\begin{bmatrix} V(z) \\ \Psi(z) \end{bmatrix} = \begin{bmatrix} C_1 \\ D_1 \end{bmatrix} \sin az + \begin{bmatrix} C_2 \\ D_2 \end{bmatrix} \cos az + \begin{bmatrix} C_3 \\ D_3 \end{bmatrix} \sinh bz + \begin{bmatrix} C_4 \\ D_4 \end{bmatrix} \cosh bz. \tag{3.21}$$

The expressions for the two dimensionless wave numbers for this case are given by the following expressions [39].

$$a = \sqrt{\left(I + \frac{1}{k'G}\right)\frac{\rho\omega^2}{2} + \sqrt{\left(I - \frac{1}{k'G}\right)^2 \frac{\rho^2\omega^4}{4} + \rho A\omega^2}} \tag{3.22}$$

$$b = \sqrt{-\left(I + \frac{1}{k'G}\right)\frac{\rho\omega^2}{2} + \sqrt{\left(I - \frac{1}{k'G}\right)^2 \frac{\rho^2\omega^4}{4} + \rho A\omega^2}} \tag{3.23}$$

Although it seems that there are now eight unknown constants to solve for the Timoshenko beam model, the C_i and D_i values are related to each other and thus only four unknowns need to be determined for the full solution [39]. The relationships between these factors are given below.

$$D_1 = -\frac{k^k GAa^2 + \rho A\omega^2}{k^k GAa} C_2 \qquad D_2 = \frac{k^k GAa^2 - \rho A\omega^2}{k^k GAa} C_1$$

$$D_3 = \frac{k^k GAb^2 + \rho A\omega^2}{k^k GAb} C_4 \qquad D_4 = \frac{k^k GAb^2 + \rho A\omega^2}{k^k GAb} C_3 \tag{3.24}$$

The equations are slightly different for the case when $\omega > \omega_C$. The spatial solutions become [39]

$$\begin{bmatrix} V(z) \\ \Psi(z) \end{bmatrix} = \begin{bmatrix} \bar{C}_1 \\ \bar{D}_1 \end{bmatrix} \sin az + \begin{bmatrix} \bar{C}_2 \\ \bar{D}_2 \end{bmatrix} \cos az + \begin{bmatrix} \bar{C}_3 \\ \bar{D}_3 \end{bmatrix} \sinh \bar{b}z + \begin{bmatrix} \bar{C}_4 \\ \bar{D}_4 \end{bmatrix} \cosh \bar{b}z. \tag{3.25}$$

The expression for the dimensionless wave number, *a*, is the same as for the previous case. The equation for $\bar{b}$ is slightly different, though, and is given by

$$\bar{b} = \sqrt{\left(I + \frac{1}{k'G}\right)\frac{\rho\omega^2}{2} - \sqrt{\left(I - \frac{1}{k'G}\right)^2 \frac{\rho^2\omega^4}{4} + \rho A\omega^2}}. \tag{3.26}$$

The constants $\bar{C}_i$ and $\bar{D}_i$ are also interrelated for the case of $\omega > \omega_C$, so there are still only four unknowns for this case. These relationships are expressed as [39]

$$\begin{aligned} \bar{D}_1 &= -\frac{k'GAa^2 + \rho A\omega^2}{k'GAa}\bar{C}_2 & \bar{D}_2 &= \frac{k'GAa^2 - \rho A\omega^2}{k'GAa}\bar{C}_1 \\ \bar{D}_3 &= -\frac{k'GA\bar{b}^2 + \rho A\omega^2}{k'GA\bar{b}}\bar{C}_4 & \bar{D}_4 &= -\frac{k'GA\bar{b}^2 - \rho A\omega^2}{k'GA\bar{b}}\bar{C}_3. \end{aligned} \tag{3.27}$$

The dimensional wave numbers *b* and $\bar{b}$ are also related through the following equation.

$$b = \mathrm{i}\,\bar{b} \tag{3.28}$$

All these relationships, along with the spatial solutions, can be combined with known boundary conditions for varying support conditions to find the mode shapes and frequency equations for different beam cases. The boundary conditions provided in the previous section need to be updated to be compatible with the spatial solution, similar to the Euler-Bernoulli and Rayleigh models. This is simply done for the Timoshenko model by changing partial derivatives to ordinary, replacing $\alpha(z, t)$ with $\Psi(z)$, and replacing $v(z, t)$ with $V(z)$.

3.3.4 Linear Elasticity Theory

The formulation for the mode shape and frequency solutions through a three-dimensional linear elasticity theory differs significantly from the three one-dimensional theories previously discussed. Rather than using an assumed displacement field, governing differential equations, and spatial solutions, Ritz-based approximations are used to solve Hamilton's principle. The details of this are presented in the following paragraphs.

Constitutive Relationship

In order to consider all three dimensions, including the Poisson effect, the development of this theory begins with the generalized Hooke's Law. This constitutive relationship in indicial form is given as

$$\sigma_{ij} = C_{ijkl}\in_{lk} \tag{3.29}$$

where σij represents the stress tensor, C_{ijkl} is the elastic stiffness tensor, and $_{kl}$ is the strain tensor. In this full form, there are nine stress and strain components and 81 stiffness terms. This would pose a very complicated problem, but fortunately the problem can be significantly simplified. Using the principle of symmetry, it can be shown that $\sigma ij = \sigma ji$ and $\in_{kl} = \in_{lk}$. This reduces the problem to six stress and strain components and only 36 stiffness terms. It has also been proven that the stiffness matrix is symmetric, which reduces this number even further to 21constants. Lastly, if the considered material is orthotropic and has three planes of symmetry, the stiffness matrix only contains nine independent constants. This reduced constitutive law that will be considered in analysis can be expressed as follows:

$$\begin{Bmatrix} \sigma_{11} \\ \sigma_{22} \\ \sigma_{33} \\ \sigma_{23} \\ \sigma_{13} \\ \sigma_{12} \end{Bmatrix} = \begin{bmatrix} C_{11} & C_{12} & C_{13} & 0 & 0 & 0 \\ C_{12} & C_{22} & C_{23} & 0 & 0 & 0 \\ C_{13} & C_{23} & C_{33} & 0 & 0 & 0 \\ 0 & 0 & 0 & C_{44} & 0 & 0 \\ 0 & 0 & 0 & 0 & C_{55} & 0 \\ 0 & 0 & 0 & 0 & 0 & C_{66} \end{bmatrix} \begin{Bmatrix} \epsilon_{11} \\ \epsilon_{22} \\ \epsilon_{33} \\ \gamma_{23} \\ \gamma_{13} \\ \gamma_{12} \end{Bmatrix} \tag{3.30}$$

The variable γ in this equation represents physical shear stress, which is equivalent to 2. The elastic stiffness constants in this matrix equation are related to the basic material properties *E*, *G*, and *v* through the following equations.

$$C_{11} = C_{22} = C_{33} = \frac{E(1-\nu)}{(1+\nu)(1-2\nu)} \tag{3.31}$$

$$C_{12} = C_{13} = C_{23} = \frac{E\nu}{(1+\nu)(1-2\nu)} \tag{3.32}$$

$$C_{44} = C_{55} = C_{66} = G \tag{3.33}$$

This constitutive law will be utilized in the solution for the elasticity-based approximation.

Hamilton's Principle

For this full elasticity theory, Hamilton's principle can be written as

$$0 = -\int_0^t \int_V \{\sigma_1\delta\epsilon_1 + \sigma_2\delta\epsilon_2 + \sigma_3\delta\epsilon_3 + \sigma_4\delta\epsilon_4 + \sigma_5\delta\epsilon_5 + \sigma_6\delta\epsilon_6\}dVdt + \frac{1}{2}\delta\int_0^t \int_V \rho(\dot{u}^2 + \dot{v}^2 + \dot{w}^2)dVdt \tag{3.34}$$

where $\dot{u} = \partial u/\partial t$ and the conventional notation for stress ($\sigma_{11} = \sigma_1$, $\sigma_{23} = \sigma_4$, etc.) has been used [44].

For this advanced beam model, selected displacement approximation functions will be used to find a solution to the above equation, rather than using potential and kinetic energy equations based upon an assumed one-dimensional displacement field and a few included displacement effects. Approximations are used because of the difficulty in finding an exact solution to the free vibration of a three-dimensional solid. The above equation only contains displacement variables in the second integral, and only stress and strain terms are found in the first integral. To determine expressions for these stress and strain terms, strain-displacement relationships are utilized as well as the constitutive law discussed previously. The basic strain-displacement equation that is utilized for this analysis for small displacements is given as

$$\epsilon_{ij} = \frac{1}{2}\left(\frac{\partial u_i}{\partial x_j} + \frac{\partial u_j}{\partial x_i}\right). \tag{3.35}$$

The strains found from this relation are used as the δ terms in Hamilton's equation. These strain expressions can then be substituted into the constitutive law to determine the stress expressions. For this study, Ritz-based approximations will be utilized for the displacement functions and are explained in the next section.

Ritz Approximations

The namesake for the Ritz method comes from Walther Ritz, who was a Swiss theoretical physicist. When Ritz was working with the bending of rectangular plates, he proposed approximation functions in the form of a finite series [40]. When used for displacement, the general form for the three direction component approximations can be written as

$$\begin{aligned} u(x,y,z,t) &= \phi_o^u(x,y,z) + \sum_{j=1}^{\cdot} c_j(t)\phi_j^u(x,y,z) \\ v(x,y,z,t) &= \phi_o^v(x,y,z) + \sum_{j=1}^{m} d_j(t)\phi_j^v(x,y,z) \\ w(x,y,z,t) &= \phi_o^v(x,y,z) + \sum_{j=1}^{n} e_j(t)\phi_j^w(x,y,z). \end{aligned} \tag{3.36}$$

In these equations *c*, *d*, and *e* are unknown constants that depend on time. The φ_o terms represent the simplest functions that satisfy the essential boundary conditions for that displacement direction. In the study discussed in this paper, the initial boundary conditions are assumed to be zero, with no initial displacement or velocity. The φ_o terms are therefore all equal to zero for the considered case. In these approximation equations, φ_j represents a selected approximate function for each respective direction. These functions must fulfill the three following requirements.

1. They satisfy the homogeneous form of the essential boundary conditions.
2. They are linearly independent of each other.
3. They must become increasingly more complex from the first term to the last used.

These Ritz-based approximations will be substituted into the equation for Hamilton's principle presented before to calculate a spatial solution. By using a large number of approximation terms for each displacement component, very accurate solutions can be determined for the mode shapes and frequencies of vibration for a beam. When the substitution into Hamilton's principle equation is done and harmonic motion is assumed, the problem is reduced to a generalized eigenvalue problem expressed as follows.

$$\begin{bmatrix} [K^{11}] & [K^{12}] & [K^{13}] \\ [K^{21}] & [K^{22}] & [K^{23}] \\ [K^{31}] & [K^{23}] & [K^{33}] \end{bmatrix} \begin{Bmatrix} \{c\} \\ \{d\} \\ \{e\} \end{Bmatrix} = \omega^2 \begin{bmatrix} [M^{11}] & 0 & 0 \\ 0 & [M^{22}] & 0 \\ 0 & 0 & [M^{33}] \end{bmatrix} \begin{Bmatrix} \{c\} \\ \{d\} \\ \{e\} \end{Bmatrix} \qquad (3.3$$

The elements of the stiffness ([*K*]) and mass ([*M*]) matrices are related to the Ritz approximations used and some basic material properties of the beam that is considered. The stiffness matrix is symmetric, so there are only six different equations for those elements. The mass matrix is diagonalized so there are only three different forms. All of these formulas are given below.

$$K_{ij}^{11} = \int_V \left(C_{11} \frac{\partial \phi_i^u}{\partial x} \frac{\partial \phi_j^u}{\partial x} + C_{55} \frac{\partial \phi_i^u}{\partial z} \frac{\partial \phi_j^u}{\partial z} + C_{66} \frac{\partial \phi_i^u}{\partial y} \frac{\partial \phi_j^u}{\partial y} \right) dV \tag{3.38}$$

$$K_{ij}^{12} = \int_V \left(C_{12} \frac{\partial \phi_i^u}{\partial x} \frac{\partial \phi_j^v}{\partial y} + C_{66} \frac{\partial \phi_i^u}{\partial y} \frac{\partial \phi_j^v}{\partial x} \right) dV = K_{ji}^{21} \tag{3.39}$$

$$K_{ij}^{13} = \int_V \left(C_{13} \frac{\partial \phi_i^u}{\partial x} \frac{\partial \phi_j^w}{\partial z} + C_{55} \frac{\partial \phi_i^u}{\partial z} \frac{\partial \phi_j^w}{\partial x} \right) dV = K_{ji}^{31} \tag{3.40}$$

$$K_{ij}^{22} = \int_V \left(C_{22} \frac{\partial \phi_i^v}{\partial y} \frac{\partial \phi_j^v}{\partial y} + C_{44} \frac{\partial \phi_i^v}{\partial z} \frac{\partial \phi_j^v}{\partial z} + C_{66} \frac{\partial \phi_i^v}{\partial x} \frac{\partial \phi_j^v}{\partial x} \right) dV \tag{3.41}$$

$$K_{ij}^{23} = \int_V \left(C_{23} \frac{\partial \phi_i^v}{\partial y} \frac{\partial \phi_j^w}{\partial z} + C_{44} \frac{\partial \phi_i^v}{\partial z} \frac{\partial \phi_j^w}{\partial y} \right) dV = K_{ji}^{32} \tag{3.42}$$

$$K_{ij}^{33} = \int_V \left(C_{33} \frac{\partial \phi_i^w}{\partial z} \frac{\partial \phi_j^w}{\partial z} + C_{44} \frac{\partial \phi_i^w}{\partial y} \frac{\partial \phi_j^w}{\partial y} + C_{55} \frac{\partial \phi_i^w}{\partial x} \frac{\partial \phi_j^w}{\partial x} \right) dV \tag{3.43}$$

$$M_{ij}^{11} = \int_V \rho \phi_i^u \phi_j^u dV \tag{3.44}$$

$$M_{ij}^{22} = \int_V \rho \phi_i^v \phi_j^v dV \tag{3.45}$$

$$M_{ij}^{33} = \int_V \rho \phi_i^w \phi_j^w dV$$

(3.46)

The general form for the Ritz approximation functions will differ for each of the different support conditions that will be considered. The primary base for all of the function employed is a simple power function. The most basic form of this is given as

$$\varphi_i(x, y, z) = x^j y^k z^l.$$

These type of functions provide simplicity when evaluating integrals over a parallelepiped. Different terms were included to ensure proper support conditions, but power functions were utilized as much as possible. When any combination of values for *j*, *k*, and *l* is considered, these power functions can represent any type of vibrational mode. If all possible combinations are evaluated, the results will include flexural vibration, shear vibration, and torsional vibration modes about all three axes. For the purposes of the investigation performed for this work, only the transverse flexural modes were of interest. To simplify and reduce the calculations required, group theory was utilized. Group theory splits all the possible Ritz functions into eight different symmetry groups [45]. Parallelepipeds contain three symmetry planes which intersect each other at right angles. Using these symmetry planes, the possible displacement patterns can be separated by considering specific combinations of odd or even behavior for each dimension about these planes. For example, half the groups follow the pattern that the *u* displacement is odd in *x*, even in *y*, and even in *z*. Therefore only odd integers will be considered for *j* and only even integers for *k* and *l*. The *v* and *w* deformation patterns can be split similarly, and through this certain modes of vibration can be isolated. Therefore, for the calculations performed for this paper, only two groups, which represent the transverse flexural vibration modes were considered [45]. This isolation of the flexural modes was possible for all three support conditions which were studied.

The three cases that were considered for the study in this paper are fixed-free, fixed-fixed, and simply supported. The Ritz functions that were used for each of these, as well as the frequency equations for the three one-dimensional beam theories, will be presented in the following sections.

3.3.5 Fixed-Free Beam

Although there are 10 different end condition combinations using symmetric and antisymmetric modes, these can be reduced to four cases. These are free-free, fixed-free (cantilevered), hinged-hinged (simply supported), and fixed-fixed [39]. An in-depth study of when the typical beam theories fail for the free-free case has already been conducted and will not be considered for this paper. Thus only three different support combinations need to be analyzed to determine a full picture of when the three one-dimensional theories are insufficient. The frequency equations that will be used for analysis of the Euler-Bernoulli, Rayleigh, and Timoshenko models were developed by Han and co-workers [39]. Each of these equations will be reiterated in this summary for reference.

The first case considered will be the cantilevered beam. When the boundary condition discussed in the previous section was substituted into the spatial solutions, the frequency equations for the free-free case were found for each of the three one-dimensional theories.

Euler-Bernoulli

For the Euler-Bernoulli case, the frequency equation is expressed as

$$\cos a \cosh a - 1 = 0. \tag{3.47}$$

For this beam model, because the relationship between the dimensionless wave number and the frequency is so simple, the frequency can be found directly using the following equation [39].

$$\omega^* = \sqrt{\frac{E^* I^*}{\rho^* A^* L^{*4}}} a^2 \tag{3.48}$$

The *s in this equation signify that these parameters are no longer dimensionless. The dimensionless wave numbers for the first five modes of vibration were found and are listed below [39].

Table 3.1 Euler-Bernoulli Wave Numbers for Fixed-Free Beam

a_1	a_2	a_3	a_4	a_5
1.875	4.694	7.855	10.996	14.137

These values were used to find the first five frequencies of vibration for beams with varying slenderness ratios, which are compared with the values from the other beam models.

Rayleigh

The frequency equation for a cantilevered beam using the Rayleigh beam model is given by [39]

$$(b^6 - a^6)\sin a \sinh b + 2a^3b^3 \cos a \cosh b - 2a^3b^3 = 0. \tag{3.49}$$

Because this model involves two wave numbers, the process to find the frequency values is not as simple. The equation for the natural frequency in terms of these two wave numbers is expressed as

$$\omega^2 = \frac{a^2 - b^2}{\rho I}. \tag{3.50}$$

To simplify the calculation, the wave number b is expressed in terms of a by the relation

$$b = a\sqrt{\frac{1}{a^2k^2 + 1}}. \tag{3.51}$$

where k is equal to $1/s$ and s is the slenderness ratio, which is given by [39]

$$s = L^*\sqrt{\frac{A^*}{I^*}}. \tag{3.52}$$

There are now two equations with three unknowns, so an iterative process is utilized to converge to the accurate wave numbers and natural frequencies. This process has been performed for multiple beams of varying slenderness ratio. The first five frequencies are then compared to the other considered beam models.

Timoshenko

Two frequency equations are necessary for the Timoshenko beam model due to the two different frequency cases discussed in the previous section. The frequency equation for a fixed-free beam when $\omega < \omega_c$ is given by

$$(a^2 - b^2)\sin a \sinh b - ab\frac{a^4 + a^4\gamma^4 + 4\gamma^2a^2b^2 + b^4\gamma^4 + b^4}{(b^2 + \gamma^2a^2)(a^2 + \gamma^2b^2)}\cos a \cosh b - 2ab = 0. \tag{3.53}$$

The equation for $\omega > \omega_c$ is slightly different and is expressed by [39]

$$(a^2 + \bar{b}^2)\sin a \sin \bar{b} - a\bar{b}\frac{a^4 + a^4\gamma^4 - 4\gamma^2a^2\bar{b}^2 + \bar{b}^4\gamma^4 + \bar{b}^4}{(-\bar{b}^2 + \gamma^2a^2)(a^2 - \gamma^2\bar{b}^2)}\cos a \cos \bar{b} - 2a\bar{b} = 0. \tag{3.54}$$

Both of these equations use the term γ to simplify the equation. This term is given as

$$\gamma^2 = \frac{2(1+\nu)}{k^k}. \tag{3.55}$$

This beam model has two dimensionless wave numbers, similar to the Rayleigh theory, and the problem is again simplified by finding a relationship between these two values [39]. When $\omega < \omega_C$ this relation is

$$\frac{(\gamma^2 b^2 + a^2)(a^2\gamma^2 + b^2)}{(a^2 - b^2)(1+\gamma^2)} = s^2. \tag{3.56}$$

For the case where $\omega > \omega_c$ the relationship is expressed as

$$\frac{(-\gamma^2\bar{b}^2 + a^2)(a^2\gamma^2 - \bar{b}^2)}{(a^2 + \bar{b}^2)(1+\gamma^2)} = s^2. \tag{3.57}$$

Using these equations along with the frequency equations, an expression for the natural frequency of a beam can be found. This expression for the case where the natural frequency is less than the critical frequency is given by

$$\omega^* = \frac{1}{L^*}\sqrt{\frac{a^2 - b^2}{1+\gamma^2}}\sqrt{\frac{E^*}{\rho^*}}. \tag{3.58}$$

If the natural frequency is greater than the critical frequency, the expression for the natural frequency is [39]

$$\omega^* = \frac{1}{L^*}\sqrt{\frac{a^2 + \bar{b}^2}{1+\gamma^2}}\sqrt{\frac{E^*}{\rho^*}}. \tag{3.59}$$

With these frequency expressions and the relationships between wave numbers, there are again two equations and three unknowns for each of the two cases. An iterative process is utilized once more to converge to the correct answer through these sets of equations. By this procedure, the first five natural frequencies are found for this theory and are compared with the results from the other three beam models.

Linear Elasticity

As discussed in the previous section, the natural frequencies and modes shapes for the linear elasticity model will be found by solving a general eigenvalue problem. Suitable Ritz-approximations are necessary to determine the matrix values for this eigenvalue problem. For the case of a cantilever beam, the following general form for the Ritz equations is used.

$$\varphi_i = x^j y^k z^l \qquad\qquad l > 0 \tag{3.60}$$

For this beam case, the same approximation can be utilized for *u*, *v*, and *w* since the boundary constraints are identical for all three direction components. For this support case, the number of Ritz terms used to express each of the displacement components is set by the parameter $j + k + l = 16$, which provides very accurate frequency results.

3.3.6 Fixed-Fixed Beam

Using the boundary conditions discussed for a fixed support at both ends of a beam, the frequency equations have been determined for each of the three typical beam theories. A different form of Ritz-based approximations has also been found for the application of a fixed-fixed beam. These equations will be presented in the following paragraphs.

Euler-Bernoulli

The frequency equation for a fixed-fixed beam using the Euler-Bernoulli model is given by

$$\cos a \cosh a - 1 = 0. \tag{3.61}$$

The equation for the natural frequency in terms of the dimensionless wave number *a* is identical to that used for the cantilever beam. The first five wave numbers for this support case have been developed by Han and co-workers and are given below [39].

Table 3.2 Euler-Bernoulli Wave Numbers for Fixed-Fixed Beam

a_1	a_2	a_3	a_4	a_5
4.730	7.853	10.996	14.137	17.279

The first five natural frequencies using these values have been calculated and are compared to the other three discussed beam models.

Rayleigh

The frequency equation using fixed boundary conditions at both ends of a beam for the Rayleigh model is expressed as [39]

$$(b^6 - a^6)\sin a \sinh b + 2a^3b^3 \cos a \cosh b - 2a^3b^3 = 0. \tag{3.62}$$

The process of determining the natural frequencies and the equations used for this procedure are the same as discussed in the fixed-free beam case. Using an iterative process, the dimensionless wave numbers and frequencies for the first five modes of vibration have been determined and compared with the other beam theories.

Timoshenko

For the case of $\omega < \omega_c$, the frequency equation using the Timoshenko beam model is expressed as

$$\frac{(a^2 - b^2)(\gamma^2 a^2 + \gamma^2 b^2 + \gamma^2 ab - ab)(\gamma^2 a^2 + \gamma^2 b^2 - \gamma^2 ab + ab)}{2ab(b^2 + \gamma^2 a^2)(a^2 + \gamma^2 b^2} \sin a \sinh b - \cos a \cosh b + 1 = 0. \tag{3.63}$$

If $\omega > \omega_c$, the frequency equation becomes

$$\frac{(a^2 - \bar{b}^2)[(\gamma^2 a^2 - \gamma^2 \bar{b}^2)^2 + (\gamma^2 a\bar{b} - a\bar{b})^2]}{2a\bar{b}(-\bar{b}^2 + \gamma^2 a^2)(a^2 - \gamma^2 \bar{b}^2)} \sin a \sin \bar{b} - \cos a \cos \bar{b} + 1 = 0. \tag{3.64}$$

The expression for the natural frequency is identical to that presented for the fixed-free beam case [39]. Using this equation and the frequency equation, the first five natural frequencies were found using an iterative process similar to that discussed for the cantilever beam.

Linear Elasticity

The general form of the Ritz approximation terms is similar to that of the fixed-free case, but it has been altered to fulfill the proper fixed end boundary conditions at the second end. The origin of the axes is again set at one end of the beam, so the approximation terms for this support case need to provide zero displacement and slope at $z = 0$ and $z = L$. The general form that was selected to allow for this is given as

$$\varphi_i = x^j y^k z^l (z - L)^2 . \tag{3.65}$$

This approximation form can again be used for all three direction components, u, v, and w, for the fixed-fixed beam case since the boundary conditions are the same for all three directions in a fixed end. The same parameter of $j + k + l = 16$ that was used to determine the number of terms in the approximation for the cantilever beam is again used for the fixed-fixed beam. This provides for very accurate frequency and mode shape solutions when the general eigenvalue problem is solved for the linear elasticity beam model. These solutions will be compared with the typical theories to understand how the assumptions in those theories affect their accuracy.

3.3.7 Simply Supported Beam

For the simply supported beam case, the boundary conditions of no transverse displacement and no moment are applied at both ends of the beam. Substituting these requirements into the spatial solutions allows for the determination of the frequency equation for each beam model. Ritz approximation forms for the linear elasticity model of a simply supported beam are also discussed.

Euler-Bernoulli

The frequency equation for a simply-supported beam as developed by Han and co-workers is given by [39]

$$\sin a \sinh a = 0. \tag{3.66}$$

The equation for the natural frequency from the previous two cases can also be used for this support condition. The first five dimensionless wave numbers that can be substituted into this equation are listed below [39].

Table 3.3 Euler-Bernoulli Wave Numbers for Simply Supported Beam

a_1	a_2	a_3	a_4	a_5
π	2π	3π	4π	5π

Rayleigh

For the Rayleigh beam model, the simply supported frequency equation is expressed as [39]

$$\sin a \sinh b = 0. \tag{3.67}$$

Using the relation between wave numbers and the equation for natural frequency presented before, the first five natural frequencies have been found through iteration to converge on the solution. These values are compared with the other beam models for the simply supported case.

Timoshenko

When the natural frequency is less than the critical value, the frequency equation for a simply supported beam using the Timoshenko theory is identical to the Rayleigh model equation as seen below.

$$\sin a \sinh b = 0 \tag{3.68}$$

For the case when the frequency is greater than ω_c the frequency equation is given by [39]

$$\sin a \sin \bar{b} = 0. \tag{3.69}$$

With the natural frequency equation that was presented for the two cases in the Timoshenko model, the above frequency equations can be used to determine the first five modes of vibration. An iterative procedure is again utilized to converge to the solutions for the simply supported case. These solutions are compared with the other models, especially the linear elasticity case, to study the accuracy of this beam model.

Linear Elasticity

The Ritz-based approximations for a simply supported beam are significantly different than for the other two support cases considered, because the constraints are not the same for all three direction components for a hinged end. Therefore, the same general form of approximation terms cannot be employed for all three directions. Another considerable difference for the simply supported case comes from the inability to satisfy the necessary boundary conditions through a power series. In order to satisfy these conditions and still have the ability to simply evaluate the functions over a parallelepiped, trigonometric functions are utilized for the axial dimension. Sine functions are used for the transverse and out-of-plane displacements, and cosine terms will be employed for the axial displacement. The type of trigonometric function that is used for each displacement component was determined by studying the displacement patterns from a finite element analysis of simply supported beam. With all these considerations, the form of the approximations

are as follows.

$$\phi_i^u = x^j y^k \sin\left(\frac{l\pi z}{L}\right) \tag{3.70}$$

$$\phi_i^v = x^j y^k \sin\left(\frac{l\pi z}{L}\right) \tag{3.71}$$

$$\phi_i^w = x^j y^k \cos\left(\frac{l\pi z}{L}\right) \tag{3.72}$$

φ

A slightly different parameter of $j + k + l = 14$ was used to set the number of terms used in the approximation for each displacement coordinate. This was changed because using a limit of $j + k + l = 16$ resulted in so many terms in each approximation that there was not enough memory on the server used for calculation to perform the analysis. The results of this linear elasticity theory are compared with the typical one-dimensional theories, particularly for less slender beams to study the accuracy of both the natural frequencies and modes shapes of vibration.

3.4 Conclusion

Four different beam theories have been presented and discussed in this chapter. Using the information presented in this chapter, a study has been conducted to investigate when three typically used, one-dimensional beam theories begin to deteriorate in accuracy. To complete this study, the three beam theories have been compared with a fully three-dimensional, linear elasticity beam model that utilizes Ritz-based approximations to calculate highly accurate natural frequencies and mode shapes for the first five modes of vibration of beams with varying dimensions. The results and conclusions from this vibration study are discussed in Section 4.

4. METHODS AND RESULTS

4.1 Introduction

A study of vibrational mechanic theories was performed to investigate their accuracy and effectiveness. This analysis was performed for three different support cases: fixed-free, fixed-fixed, and simply supported. For each of these cases, the frequencies of the first five flexural vibration modes were computed using the Euler-Bernoulli, Rayleigh, and Timoshenko beam theories, as well as a full elasticity approximation with and without the inclusion of the Poisson effect. One of the assumptions utilized in the three common theories that may cause inaccuracies is that a beam is slender. One purpose of this study was to investigate when this assumption leads to significant errors in the frequency results. Therefore, the modal frequencies were found for a variety of slenderness ratios, ranging from less than 7 to almost 350. Another item of interest in this study was how the assumption of an isotropic material affects the accuracy of typical beam theories. To investigate this, the resonant frequencies were found for both and isotropic material (steel) and an orthotropic material (graphite-magnesium). The last assumption examined in this study was that the Poisson effect was negligible. This was studied by utilizing the Ritz-based approximation with a zero Poisson ratio, as well as the typical material Poisson ratios. The results of these investigations are presented and discussed in the remainder of this section.

Also examined in this section are the results of calculations performed for a potential new infrastructure sensor. The device is a microelectromechanical system (MEMS) sensor, which will operate by exciting vibrational resonance in a small fixed-fixed bridge within the device using a microwave-frequency current. In order to properly excite the bridge, accurate resonant frequencies are needed. Using the full elasticity approximation presented in the vibrational mechanics study, the resonant frequencies for flexure in the lateral modes have been determined. This information will be useful in future testing and calibration of the device.

4.2 Vibration Study Methods

As mentioned in the previous section, the accuracy of typical beam theories was investigated by deter- mining the resonant frequencies of the first five modes for varying beam types using each theory. In order to calculate these results, computing programs were prepared for each theory and support case based upon the governing equations presented in Section 3. Each of these programs were written to allow for different beam geometries and material properties.

The assumption of one beam dimension being significantly larger than the other two was the first to be investigated. This was done by considering beams of many different lengths, and thus, varying slenderness ratios. Each calculation was done for a one-by-one cross section. The different lengths that were studied include: 2, 5, 10, 20, 40, and 100. Calculations using the three typical theories, as well as a full elasticity approximation, were performed for each of these lengths and compared. These results are discussed in the next section of this report.

The three beam theories of interest in this study also assume that the material of a beam is isotropic. An anisotropic material can be somewhat accommodated through the shear coefficient for the Timoshenko model, but all other beam theory equations do not consider the effect of anisotropy. This vibrational study, therefore, also considered the accuracy of these models when a

beam is isotropic or orthotropic. Steel was chosen as the isotropic material to study, while graphite-magnesium was utilized for an orthotropic material. The elastic constants and stiffness values for a graphite-magnesium composite were determined by H.M. Ledbetter and others [46]. These values, as well as those for steel, are given in Table 4.1.

The last item of particular interest in this study is the Poisson effect. The three theories typically used for beam analysis neglect this effect. The full elasticity approximation allows for displacements due to the Poisson effect and thus allowed for an investigation of what involvement this phenomenon has on the frequency and mode shapes of a vibrating beam. Also, to attempt to isolate the influence of the Poisson effect from the other two assumptions previously discussed, the Ritz-based elasticity approximation was used to calculate frequencies with zero v as well as the with the correct Poisson ratios listed in Table 4.1. The findings of this study are presented in the following section.

4.3 Vibration Study Results

The resonant frequencies for the first five modes were the primary results that were investigated in this vibrational mechanics study. These values were found for various lengths, materials, and support conditions.

Table 4.1 Material Properties for Vibration Study, units are GPa except for dimensionless v_{ij} and Density in kg/m^3

Constant	Steel	Graphite-Magnesium
E_1	200	23.81
E_2	200	23.81
E_3	200	166.64
v_{12}	0.3	0.359
v_{13}	0.3	0.045
v_{23}	0.3	0.045
v_{21}	0.3	0.359
v_{31}	0.3	0.314
v_{32}	0.3	0.314
C_{11}	269.23	28.19
C_{22}	269.23	28.19
C_{33}	269.23	174.30
C_{44}	76.923	17.91
C_{55}	76.923	17.91
C_{66}	76.923	8.76
C_{12}	115.38	10.67
C_{13}	115.38	12.20
C_{23}	115.38	12.20
Density, ρ	7830	1738

All the calculated frequencies can be found in the following tables. The results for a cantilever beam are listed in Table 4.2 and Table 4.3 for an isotropic and orthotropic beam, respectively. For a fixed-fixed support case, the results are provided in Table 4.4 and Table 4.5, again for isotropic or orthotropic materials. Lastly, the frequencies for a simply supported beam case are given in

Table 4.6 and Table 4.7. For most of the cases involving a fixed support, the higher mode frequencies from the Timoshenko beam model were not able to be calculated. It seems that when the slenderness ratio becomes so small, the program created to determine the Timoshenko values will not converge to an answer. Even without some of these values trends were still able to be determined and conclusions drawn. From the values found, the influence of slenderness, anistropy and the Poisson effect could be investigated. The effect of each of these factors for the different support conditions are discussed in the remainder of this section.

Table 4.2 Frequencies of an Isotropic Cantilevered Beam

L	Mode	E-B	Rayleigh	Timoshenko	$\nu = 0$	Full
	1	1282.29	1224.17	1093.04	1099.82	1149.29
	2	8036.55	6205.44	4147.35	4284.97	4313.85
2	3	22501.84	14104.63	8676.21	8898.61	8919.19
(S=6.928)	4	44101.46	22570.04	11251.97	11306.62	11320.33
	5	72895.05	31184.49	14596.18	13161.22	13396.42
	1	205.19	203.62	199.08	199.33	209.11
	2	1285.87	1221.42	1074.13	1089.48	1121.12
5	3	3600.77	3211.34	2560.16	2634.54	2681.66
(S=17.32)	4	7056.23	5812.27	4255.09	4446.58	4501.16
	5	11663.21	8811.58	6055.60	6276.84	6312.54
	1	51.297	51.198	50.900	50.924	53.452
	2	321.467	317.215	305.250	307.096	318.146
10	3	900.193	872.477	803.480	815.589	836.107
(S=34.64)	4	1764.058	1667.443	1458.715	1501.403	1526.117
	5	2915.805	2673.048	2222.277	2382.836	2407.668
	1	12.824	12.818	12.799	12.803	13.440
	2	80.367	80.099	79.291	79.570	82.617
20	3	225.048	223.244	218.069	220.133	226.432
(S=69.28)	4	441.015	434.556	416.846	425.520	433.694
	5	728.951	712.239	668.673	712.071	719.086
	1	3.2061	3.2057	3.2045	3.2053	3.3647
	2	20.0917	20.0752	20.0237	20.0807	20.8626
40	3	56.2621	56.1457	55.8054	56.2424	57.9127
(S=138.56)	4	110.2536	109.8364	108.6221	110.5882	112.8251
	5	182.2378	181.1688	178.0269	189.1699	190.9816
	1	0.51297	0.51296	0.51293	0.51305	0.53857
	2	3.21467	3.21431	3.21298	3.22153	3.34755
100	3	9.00193	8.99848	8.98964	9.05576	9.32763
(S=346.41)	4	17.64058	17.62862	17.59666	17.90082	18.26871
	5	29.15805	29.13104	29.04698	30.84565	31.13821

Table 4.3 Frequencies of an Orthotropic Cantilevered Beam

L	Mode	E-B	Rayleigh	Timoshenko	$\nu = 0$	Full
	1	2484.37	2371.78	1703.94	1729.30	1738.72
	2	15570.42	12022.72	5434.23	5548.43	5556.60
2	3	43602.01	27327.02	-	9726.02	9801.51
(S=6.928)	4	85444.40	43728.35	-	10818.68	10871.55
	5	141230.55	60418.40	-	11667.13	11715.13
	1	397.50	394.50	365.77	366.76	369.45
	2	2491.27	2366.44	1659.44	1707.68	1713.45
5	3	6976.32	6221.81	3603.82	3708.18	3715.05
(S=17.32)	4	13671.10	11260.99	5570.92	5677.38	5688.80
	5	22596.89	17072.00	7556.90	7700.27	7714.03
	1	99.375	99.194	97.203	97.281	98.043
	2	622.817	614.588	542.805	549.257	551.907
10	3	1744.080	1690.380	1324.954	1359.684	1364.268
(S=34.64)	4	3417.776	3230.588	2240.531	2335.581	2342.316
	5	5649.222	5178.898	3220.536	3337.431	3343.200
	1	24.844	24.834	24.707	24.715	24.912
	2	155.704	155.187	148.884	150.658	151.499
20	3	436.020	432.524	400.108	405.525	407.119
(S=69.28)	4	854.444	841.931	737.033	757.386	759.503
	5	1412.305	1379.927	1136.833	1219.862	1222.479
	1	6.2109	6.2109	6.2028	6.2044	6.2540
	2	38.9260	38.8947	38.5475	38.6736	38.8988
40	3	109.0050	108.7795	106.5160	107.4695	107.9194
(S=138.56)	4	213.6110	212.8027	204.8697	208.9977	209.5795
	5	353.0764	351.0056	330.9243	352.5038	353.0551
	1	0.99375	0.99384	0.99363	0.99385	1.00182
	2	6.22817	6.22757	6.21856	6.23551	6.27229
100	3	17.44080	17.43411	17.37419	17.50519	17.57998
(S=346.41)	4	34.17776	34.15457	33.93870	34.53706	34.63319
	5	56.49222	56.43994	55.87438	59.35934	59.43626

Table 4.4 Frequencies of an Isotropic Fixed-Fixed Beam

L	Mode	E-B	Rayleigh	Timoshenko	$\nu = 0$	Full
	1	8160.29	7276.64	3947.00	4067.61	4156.69
	2	22493.38	16031.52	7711.15	7951.97	8016.46
2	3	44101.46	25232.54	-	12665.35	12740.30
(S=6.928)	4	72895.05	34162.23	-	17869.87	18071.29
	5	108898.19	42894.24	-	23039.24	23231.10
	1	1305.65	1279.67	1053.57	1070.31	1105.72
	2	3598.94	3350.56	2415.61	2471.41	2526.54
5	3	7056.23	6117.99	4029.29	4157.36	4224.59
(S=17.32)	4	11663.21	9302.02	5760.38	5961.74	6038.66
	5	17423.71	12708.68	7566.97	7872.99	7936.89
	1	326.412	324.756	306.315	310.131	321.455
	2	899.735	882.988	785.788	798.092	823.077
10	3	1764.059	1695.419	1421.532	1449.363	1483.411
(S=34.64)	4	2915.802	2727.330	2160.254	2212.983	2254.271
	5	4355.928	3943.480	2968.401	3067.753	3117.107
	1	81.603	81.500	80.250	81.192	84.220
	2	224.934	223.874	216.591	219.501	227.318
20	3	441.015	436.508	413.359	419.157	430.819
(S=69.28)	4	728.950	716.276	661.887	674.313	690.634
	5	1088.982	1060.184	954.204	975.394	995.855
	1	20.4007	20.3946	20.3147	20.5686	21.3294
	2	56.2334	56.1691	55.6898	56.4464	58.5207
40	3	110.2537	109.9629	108.3754	109.8344	113.0188
(S=138.56)	4	182.2376	181.4330	177.5127	180.7184	185.5264
	5	272.2455	270.3853	262.3055	267.3909	273.5839
	1	3.26412	3.26401	3.26195	3.32304	3.43547
	2	8.99735	8.99609	8.98364	9.14956	9.47477
100	3	17.64059	17.63206	17.59028	17.96247	18.44485
(S=346.41)	4	29.15802	29.13788	29.03299	29.77728	30.58208
	5	43.55928	43.51023	43.28975	44.74848	45.75155

Table 4.5 Frequencies of an Orthotropic Fixed-Fixed Beam

L	Mode	E-B	Rayleigh	Timoshenko	$\nu = 0$	Full
	1	15810.17	14098.13	4500.41	4649.87	4661.04
	2	43579.82	31060.28	8885.38	9192.75	9211.47
2	3	85444.40	48886.80	-	10574.52	10683.07
(S=6.928)	4	141230.55	66187.62	-	17038.85	16722.03
	5	210984.86	83105.47	-	21824.63	21772.46
	1	2529.63	2479.30	1508.23	1537.40	1544.50
	2	6972.77	6491.54	3135.55	3222.04	3230.33
5	3	13671.10	11853.31	5014.83	5142.33	5155.16
(S=17.32)	4	22596.89	18022.20	6937.85	7135.95	7150.96
	5	33757.58	24622.44	8885.12	9138.90	9155.73
	1	632.407	629.200	524.644	531.315	534.244
	2	1743.192	1710.746	1230.568	1253.115	1258.302
10	3	3417.776	3284.789	2080.759	2135.417	2142.921
(S=34.64)	4	5649.222	5284.067	3002.296	3089.447	3099.222
	5	8439.394	7640.297	3963.226	4120.143	4129.059
	1	158.102	157.902	149.847	151.556	152.440
	2	435.798	433.745	389.357	394.379	396.684
20	3	854.444	845.713	713.313	725.179	728.129
(S=69.28)	4	1412.305	1387.750	1096.113	1119.157	1123.014
	5	2109.849	2054.054	1519.743	1564.651	1569.730
	1	39.5254	39.5134	38.9782	39.4260	39.6587
	2	108.9495	108.8248	105.6627	107.0223	107.6105
40	3	213.6110	213.0477	202.7912	205.4340	206.3256
(S=138.56)	4	353.0764	351.5174	326.8051	332.5416	333.7862
	5	527.4621	523.8582	474.2981	484.0115	485.6946
	1	6.32407	6.32385	6.30990	6.39440	6.43117
	2	17.43192	17.42949	17.34520	17.59123	17.68912
100	3	34.17776	34.16125	33.87952	34.36394	34.51226
(S=346.41)	4	56.49222	56.45319	55.74922	56.79759	57.01745
	5	84.39394	84.29893	82.82703	84.53273	84.82903

Table 4.6 Frequencies of an Isotropic Simply-Supported Beam

L	Mode	E-B	Rayleigh	Timoshenko	$\nu = 0$	Full
	1	3599.84	3278.53	2712.61	2705.03	2688.52
	2	14399.36	10666.29	7393.83	7367.28	7286.58
2	3	32398.56	19189.40	12229.28	12199.06	12060.85
(S=6.928)	4	57597.45	27808.74	17010.07	16997.14	16831.98
	5	89996.01	36318.21	21730.55	21749.33	21584.08
	1	575.97	566.73	541.69	541.23	540.43
	2	2303.90	2165.80	1881.89	1877.67	1869.13
5	3	5183.77	4553.32	3600.91	3589.39	3562.46
(S=17.32)	4	9215.59	7459.20	5470.54	5450.81	5398.13
	5	14399.36	10666.29	7393.83	7367.28	7286.64
	1	143.994	143.405	141.662	141.629	141.572
	2	575.974	566.727	541.687	541.232	540.432
10	3	1295.943	1250.487	1142.155	1140.365	1137.004
(S=34.64)	4	2303.898	2165.797	1881.892	1877.666	1869.127
	5	3599.840	3278.826	2712.610	2705.026	2688.526
	1	35.998	35.961	35.849	35.847	35.843
	2	143.994	143.405	141.662	141.629	141.572
20	3	323.986	321.029	312.605	312.446	312.174
(S=69.28)	4	575.974	566.728	541.687	541.232	540.433
	5	899.960	877.684	820.892	819.907	818.118
	1	8.9996	8.9973	8.9902	8.9901	8.9899
	2	35.9984	35.9615	35.8494	35.8487	35.8434
40	3	80.9964	80.8097	80.2490	80.2380	80.2196
(S=138.56)	4	143.9936	143.4051	141.6625	141.6285	141.5716
	5	224.9900	223.5581	219.3924	219.3123	219.1770
	1	1.43994	1.43987	1.43970	1.43969	1.43969
	2	5.75974	5.75880	5.75590	5.75585	5.75575
100	3	12.95943	12.95463	12.94001	12.93972	12.93924
(S=346.41)	4	23.03898	23.02383	22.97776	22.97684	22.97532
	5	35.99840	35.96145	35.84935	35.84712	35.84344

Table 4.7 Frequencies of an Orthotropic Simply-Supported Beam

L	Mode	E-B	Rayleigh	Timoshenko	$\nu = 0$	Full
	1	6974.51	6351.98	3854.06	3823.95	3812.57
	2	27898.05	20665.41	8856.85	8864.57	8843.49
2	3	62770.61	37178.51	13708.31	10445.80	10573.31
(S=6.928)	4	111592.20	53878.05	18489.92	16619.39	16102.21
	5	174362.82	70364.70	21013.71	20934.36	21035.53
	1	1115.92	1098.01	950.72	946.36	945.06
	2	4463.69	4196.12	2840.57	2817.92	2810.20
5	3	10043.30	8821.84	4869.36	4836.29	4821.75
(S=17.32)	4	17854.75	14451.82	6879.00	6856.22	6837.33
	5	27898.05	20665.41	8856.85	8864.57	8843.53
	1	278.981	277.840	266.498	266.083	265.964
	2	1115.922	1098.007	950.722	946.358	945.059
10	3	2510.825	2422.757	1852.608	1839.732	1835.667
(S=34.64)	4	4463.688	4196.125	2840.571	2817.916	2810.202
	5	6974.513	6351.982	3854.063	3823.954	3812.579
	1	69.745	69.674	68.920	68.891	68.882
	2	278.981	277.840	266.498	266.083	265.964
20	3	627.706	621.978	569.658	567.917	567.410
(S=69.28)	4	1115.922	1098.007	950.722	946.358	945.059
	5	1743.628	1700.470	1384.761	1376.555	1374.045
	1	17.4363	17.4318	17.3839	17.3820	17.3815
	2	69.7451	69.6735	68.9199	68.8906	68.8823
40	3	156.9265	156.5648	152.8476	152.7067	152.6667
(S=138.56)	4	278.9805	277.8403	266.4975	266.0826	265.9642
	5	435.9070	433.1328	406.6094	405.6809	405.4136
	1	2.78981	2.78969	2.78846	2.78841	2.78839
	2	11.15922	11.15739	11.13774	11.13696	11.13673
100	3	25.10825	25.09896	24.99995	24.99604	24.99492
(S=346.41)	4	44.63688	44.60754	44.29649	44.28428	44.28081
	5	69.74513	69.67353	68.91992	68.89057	68.88225

4.3.1 Effects of Slenderness

From the results of this study, it is clear that the slenderness ratio of a beam has a significant effect on the accuracy of frequency calculations for two of the common beam theories. As the slenderness ratio decreases to a point where the solid is closer to a cube than a typical beam, the error between the elasticity solution and both the Euler-Bernoulli and Rayleigh results increases exponentially. For the Timoshenko beam model, the length of a beam has a minimal effect on the percent error from the full elasticity theory. This is especially true for the fundamental mode of an isotropic beam. The support case for a beam affects the level of accuracy for each beam theory as the slenderness ratio changes, but these general trends are consistent throughout.

For the cantilever beam and fixed-fixed beam scenarios, all three beam theories approach a similar error value as the slenderness increases. The existence of even one fixed support for a beam leads to noticeable errors in frequency for even very slender beams. This is most likely due to neglecting the Poisson effect and will be discussed in Section 4.3.3. Although the frequency results from the beam theories do not approach the full elasticity solution, they still demonstrate the slenderness trends discussed above. As the slenderness value decreases, the results for both the Euler-Bernoulli and Rayleigh models begin to deviate from the asymptotic error percentage at an exponential rate, as can be seen in Figures 4.1 and 4.3. The error values from the Rayleigh beam model are less than those from Euler-Bernoulli model calculations, as was expected, but the slenderness ratio of a beam still has a meaningful influence on the accuracy of the Rayleigh model. This effect is significantly greater for higher modes of vibration for both beam theories. While the errors for the fundamental mode of a 1x1x2 beam are 11.6% and 6.5% for Euler-Bernoulli and Rayleigh, respectively, these errors grow to 444% and 133% for the fifth mode of vibration in a cantilevered beam. The errors for a fixed-fixed beam are even larger for higher modes of vibration. The error values for the fifth mode are shown in Figures 4.2 and 4.4. The minute effect that slenderness has upon the Timoshenko frequency results can also be seen in these figures. While the other two beam theories diverge exponentially as the beam length falls below 10, the Timoshenko model remains at a very similar error value throughout the entire range of slenderness ratios considered. The error increases slightly more for very stout beams and higher modes of vibration, but this increases is small in comparison with the other two theories.

The results from a simply supported beam also follow similar trends. The main difference for this support case is that the frequency values from the three beam theories actually approach the full elasticity solutions, rather than a common error value. The error still increases significantly for the Euler-Bernoulli and Rayleigh beam theories as a beam becomes less slender, while the influence is minimal for the Timoshenko model. Slenderness is also still a greater factor for higher modes of vibration than for the fundamental mode. The error values for a simply supported beam as the beam length varies are shown in Figures 4.5 and 4.6.

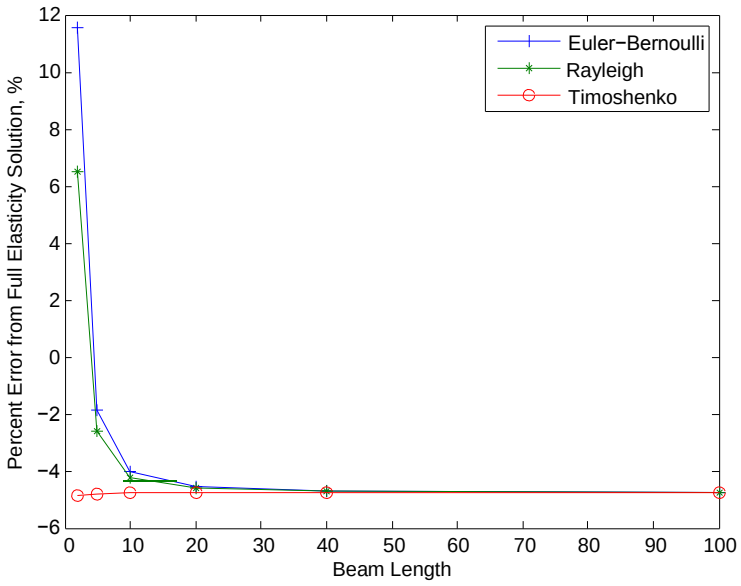

Figure 4.1 Frequency Error for the First Mode of a Cantilevered Beam

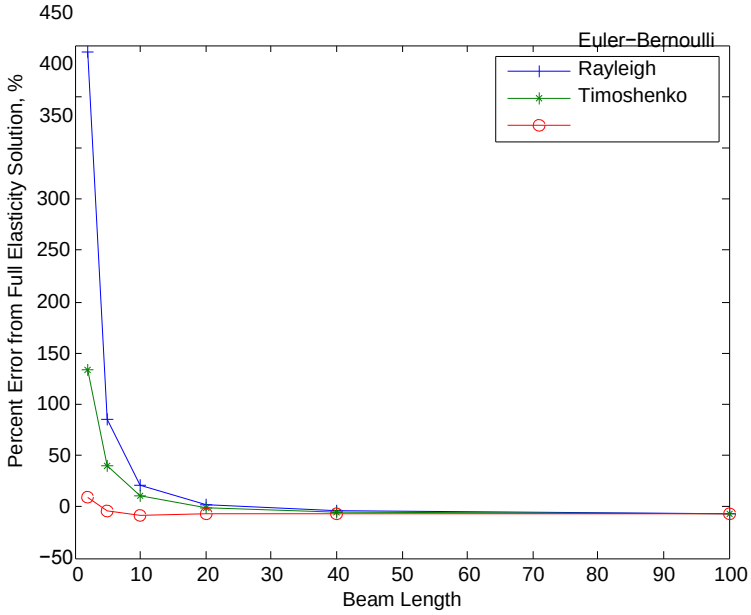

Figure 4.2 Frequency Error for the Fifth Mode of a Cantilevered Beam

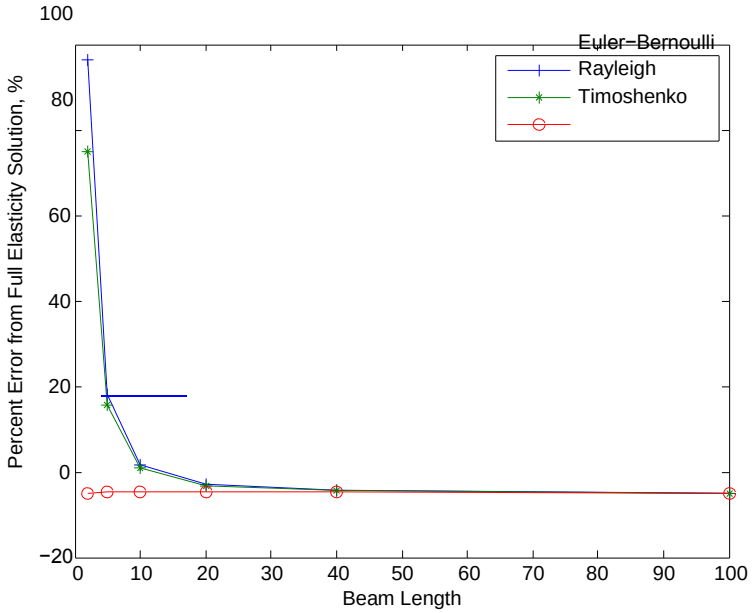

Figure 4.3 Frequency Error for the First Mode of a Fixed-Fixed Beam

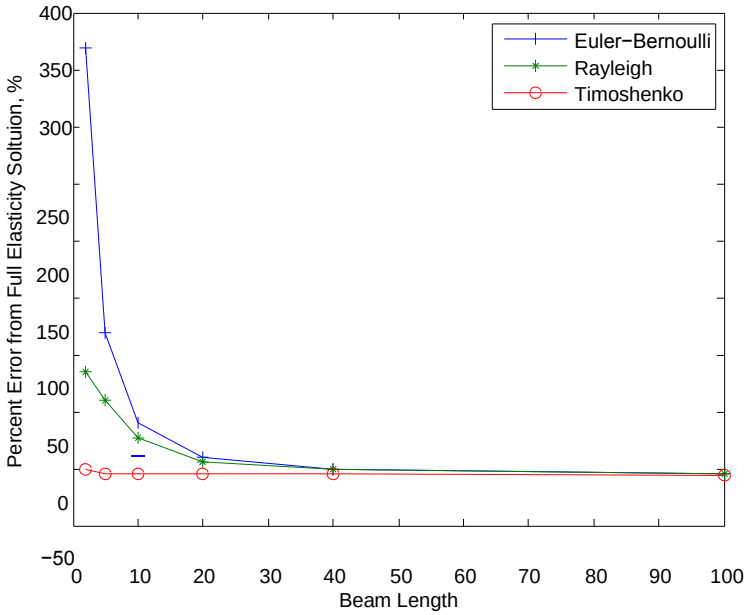

Figure 4.4 Frequency Error for the Fifth Mode of a Fixed-Fixed Beam

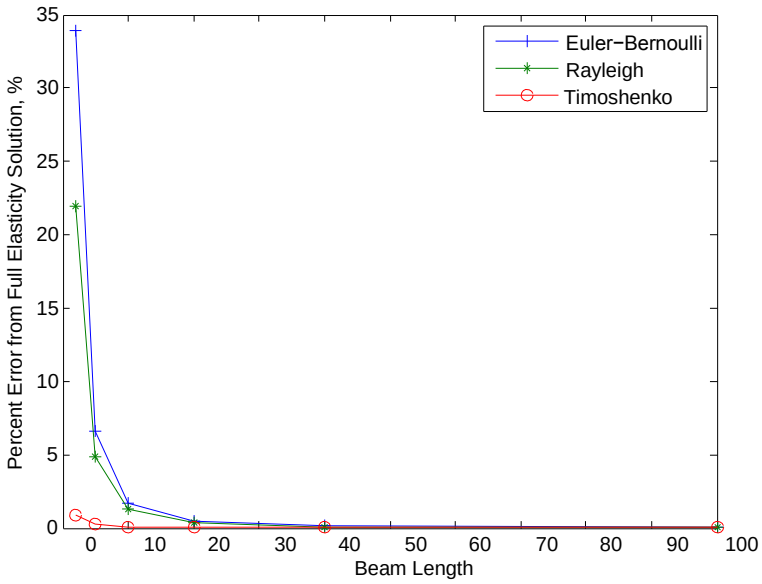

Figure 4.5 Frequency Error for the First Mode of a Simply-Supported Beam

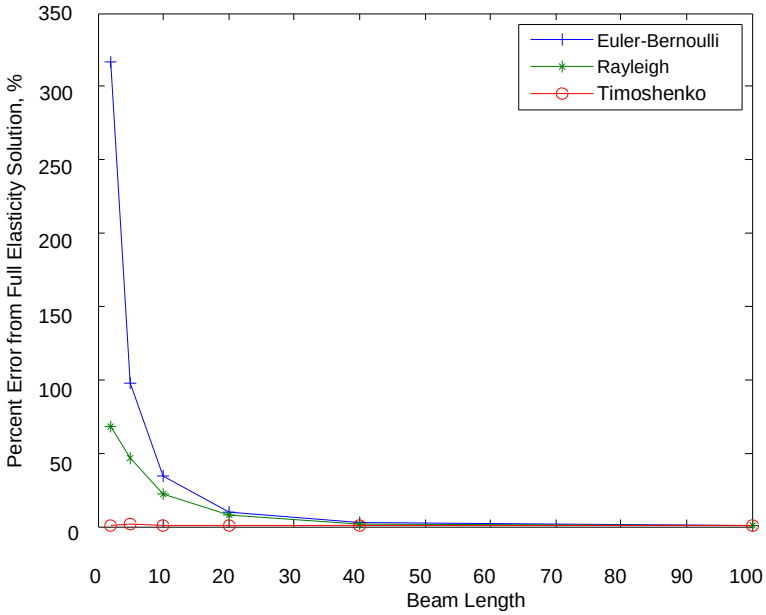

Figure 4.6 Frequency Error for the Fifth Mode of a Simply-Supported Beam

All these results follow the expected trends. As the slenderness of a beam decreases, the displacement pattern is known to deviate from the linear model that each of the three beam theories assume. For example, in the extreme case where the beam length approaches the width or becomes less than the width, the deformation pattern becomes more similar to that of a plate than a beam. It is therefore clear that the one-dimensional displacement patterns of the common beam theories cannot be applied to very short and thick beams. In this study, three-dimensional displacement patterns were determined using the Ritz-based approximation program. It was found that obvious warping of the beam surface through the width and height begins to occur for very stocky beams. When a beam is very slender, the displacement is dominant in only one dimension as the three common beam theories assume, but this deteriorates rapidly as the slenderness decreases. The first five three-dimensional mode shapes were plotted for both a very slender beam (1x1x40) and a very stout beam (1x1x2) for each of the support cases. Figures 4.7, 4.8, 4.9, 4.10, 4.11, and 4.12 show these mode shapes and how the deformation behavior drastically changes for non-slender beams. You can clearly see how the deformation pattern deviates from beam theory expectations in Figure 4.8, where the cross-sectional plane is no longer plane throughout displacement; this is especially noticeable on the free face of the fifth mode shape. In the fourth and fifth mode shape for both the fixed-fixed and simply supported cases, the Poisson effect begins to have a significant influence for very short beams. In these plots, obvious warping through the width of the beam occurs due to the shrinking and expansion influences of the Poisson ratio. The displacement patterns in these cases can no longer be accurately modeled through a one-dimensional plot of the centerline since the deformation of the outer surfaces is significantly different than what occurs at the centerline of the beam. With the very slender beams, the deformation follows typical beam theory expectations with the entire cross section of the beam moving essentially as one. In very slender beam cases, it is therefore acceptable to use a one dimensional centerline displacement to model beam vibrations. Three dimensional mode shapes are necessary though for low slenderness ratios to capture the accurate displacements.

An unexpected result did arise when creating the three-dimensional modal deformation plots. For most beams, the lower modes of vibrational are always flexural, but it was found that for very non-slender beams this was not the case. When determining the mode shapes for the 1x1x40 beam, the lowest five modal frequencies were clearly flexural modes and matched exactly the expected displacement patterns. For the very short beam case, the lowest three modes followed flexural displacements for all three support conditions, but the fourth and fifth lowest frequencies corresponded to very different deformation types. For the fixed-fixed case, the fifth flexural mode did not appear until the 14th lowest mode of vibration. This finding provides another strong reason for more accurate frequency and mode shape calculations when dealing with non-slender beams since non-flexural modes of vibration may become dominant far earlier than anticipated.

If the only factor affecting the accuracy of frequency results were slenderness, it would be clear that the Timoshenko model provides an acceptable approximation for frequencies. This model presents a significant improvement over either of the other two beam models when it comes to the loss of accuracy with less slender beams. The Rayleigh model gives improved results in comparison to Euler-Bernoulli, but the correction is minor compared to that of the Timoshenko model. The slenderness ratio of a beam is not the only element affecting the frequency results, though, so the conclusion that the Timoshenko model is adequate cannot be made. The material properties and the Poisson effect also alter the results as will be discussed in the following paragraphs.

4.3.2 Effects of Anisotropy

The slenderness ratio of a beam has arguably the greatest influence on the accuracy of frequency results, but the results of this study demonstrate that anisotropic material properties can intensify this effect. Since the three basic theories assume that a beam is composed of isotropic material, the error in frequency results increases significantly when they are applied to an orthotropic material. This is especially true for the Euler-Bernoulli and Rayleigh beam theories. Figures 4.13, 4.14, and 4.15 display this trend. The accuracy of frequency values for the orthotropic material, graphite-magnesium, decreases even more rapidly than for steel as the slenderness decreases. For example, the error is more than four times greater for the orthotropic fixed-fixed beam than the isotropic case. The error increase for an anisotropic beam becomes insignificant for very slender beams, displaying that the slenderness ratio provides the dominant influence on frequency results. Anisotropic material properties simply exacerbate the loss of accuracy at low slenderness ratios.

A result from this study, which was unexpected, comes from the Timoshenko beam model. Surprisingly, the Timoshenko model was exceptionally adaptable to the orthotropic material used. It is unclear whether this outcome is unique to graphite-magnesium or if the Timoshenko beam theory would perform well for any orthotropic or anisotropic material. More calculations would need to be completed with a larger variety of materials to answer that question. For the materials considered in this study, though, the frequency errors were very similar for both the isotropic and orthotropic material, as can be noted from Figures 4.13, 4.14, and 4.15. The fact that the Timoshenko model could accommodate an orthotropic material may be due to the influence of the shear factor. As discussed in Section 3, the shear coefficient for the orthotropic material was calculated through a number of equations that took the anisotropic material properties into account. Neither of the other two beam theories provide a means to consider anything other than isotropic properties, which may be the reason for the significant loss of accuracy when applied to an orthotropic beam.

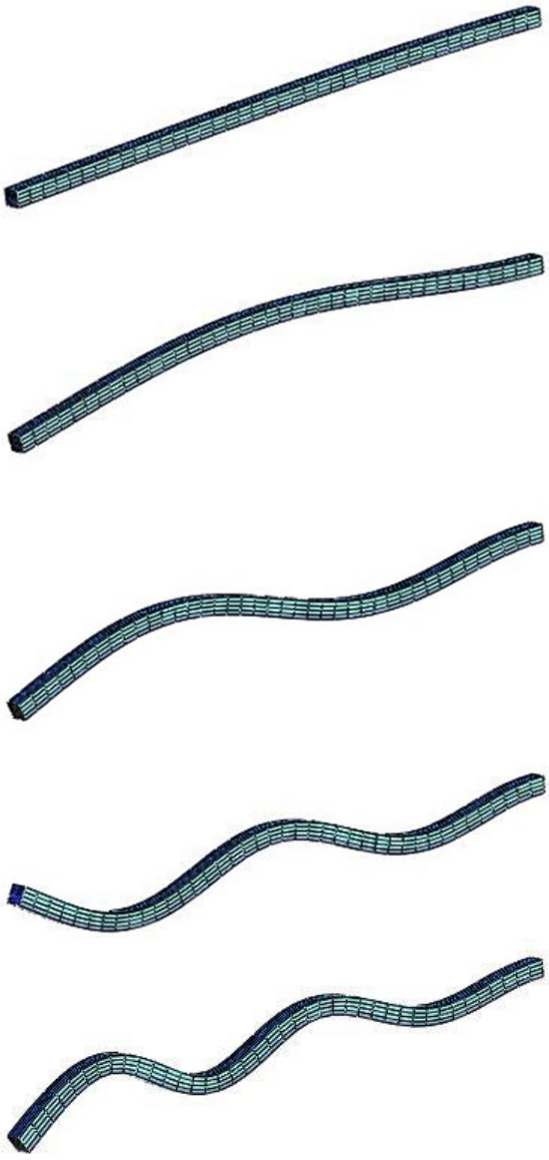

Figure 4.7 First Five Mode Shapes for a 1x1x40 Isotropic Fixed-Free Beam

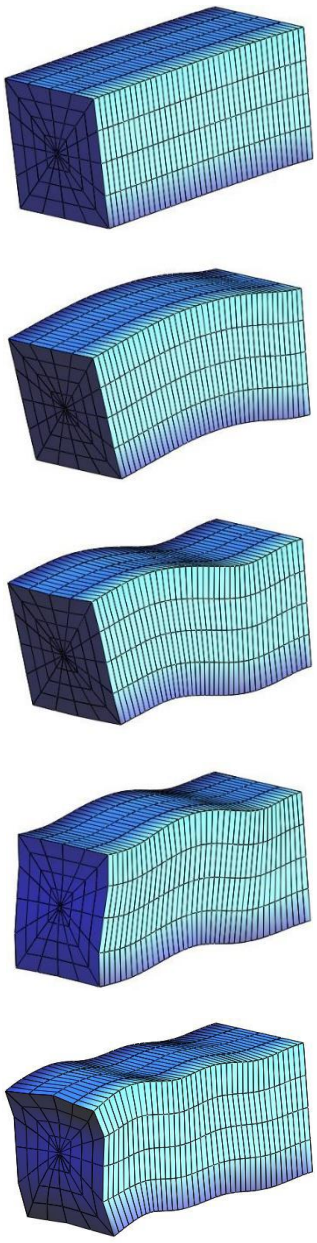

Figure 4.8 First Five Mode Shapes for a 1x1x2 Isotropic Fixed-Free Beam

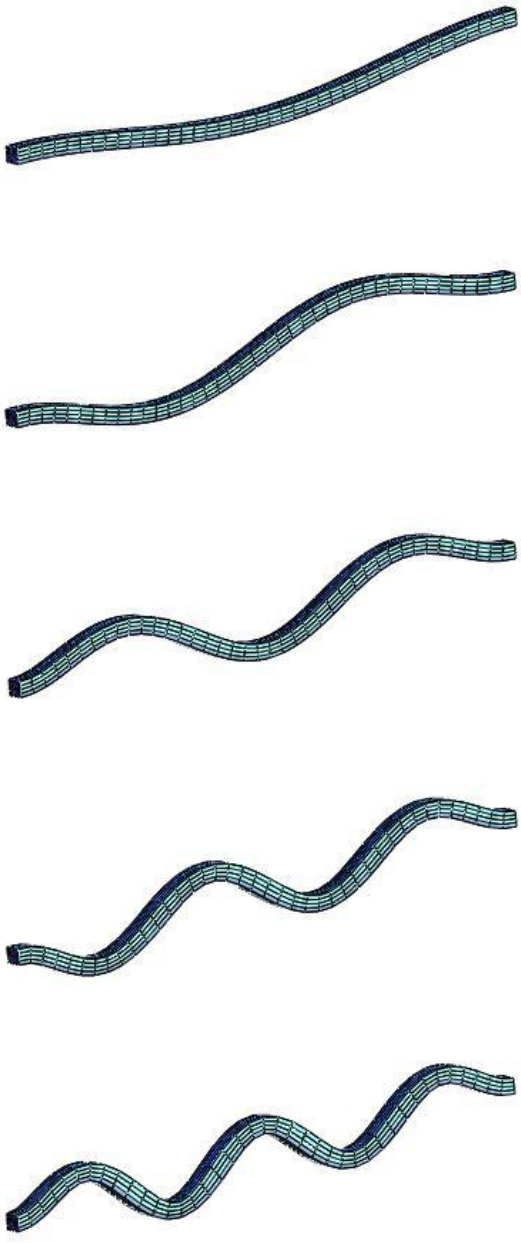

Figure 4.9 First Five Mode Shapes for a 1x1x40 Isotropic Fixed-Fixed Beam

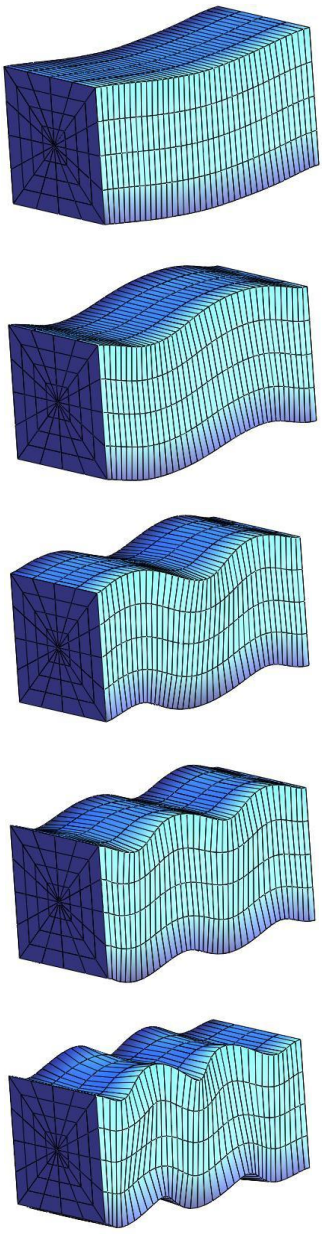

Figure 4.10 First Five Mode Shapes for a 1x1x2 Isotropic Fixed-Fixed Beam

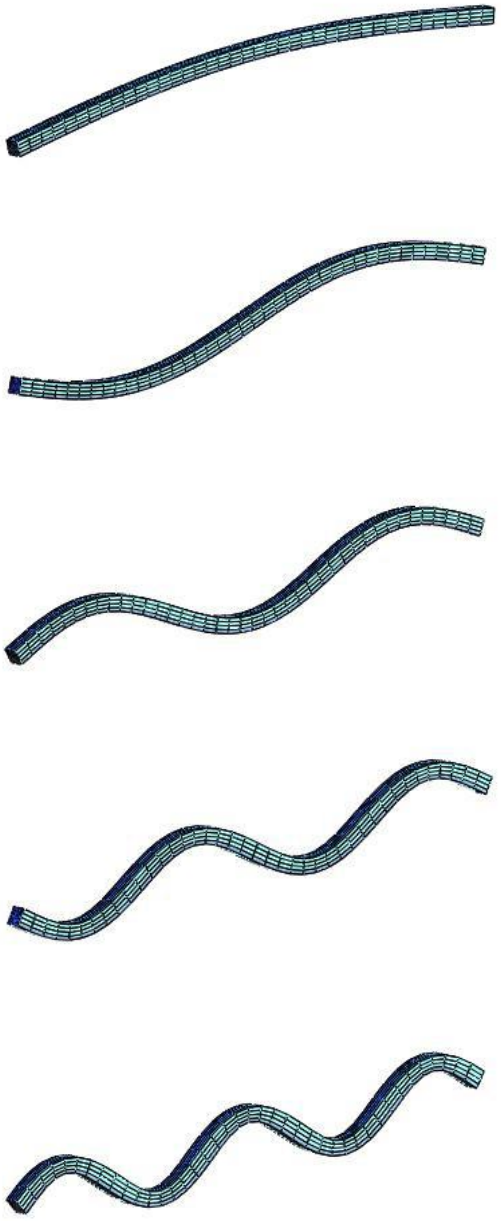

Figure 4.11 First Five Mode Shapes for a 1x1x40 Isotropic Simply-Supported Beam

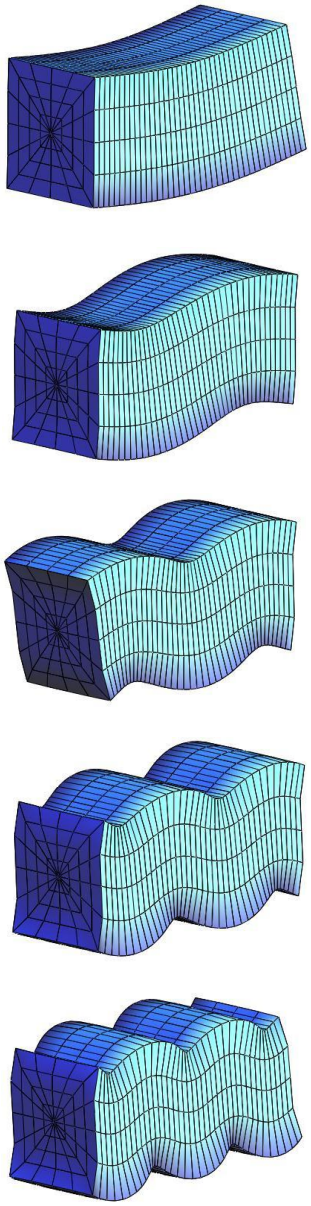

Figure 4.12 First Five Mode Shapes for a 1x1x2 Isotropic Simply-Supported Beam

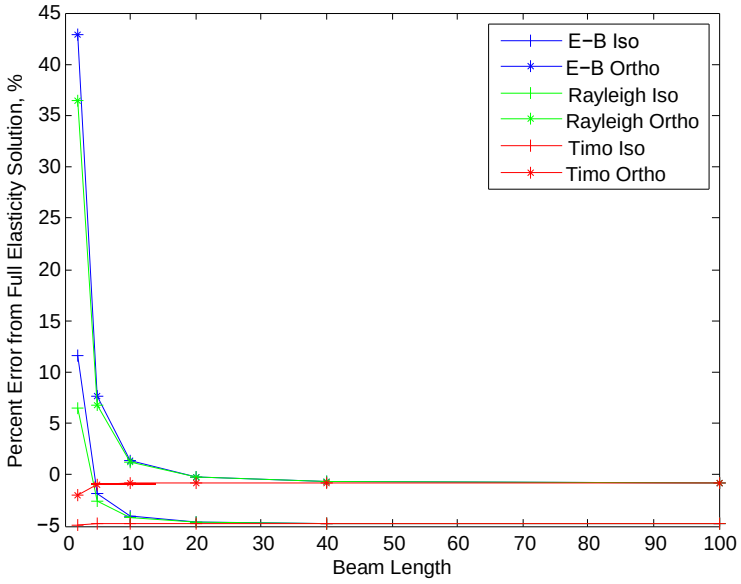

Figure 4.13 Error Comparison Between Isotropic and Orthotropic Materials for a Cantilevered Beam

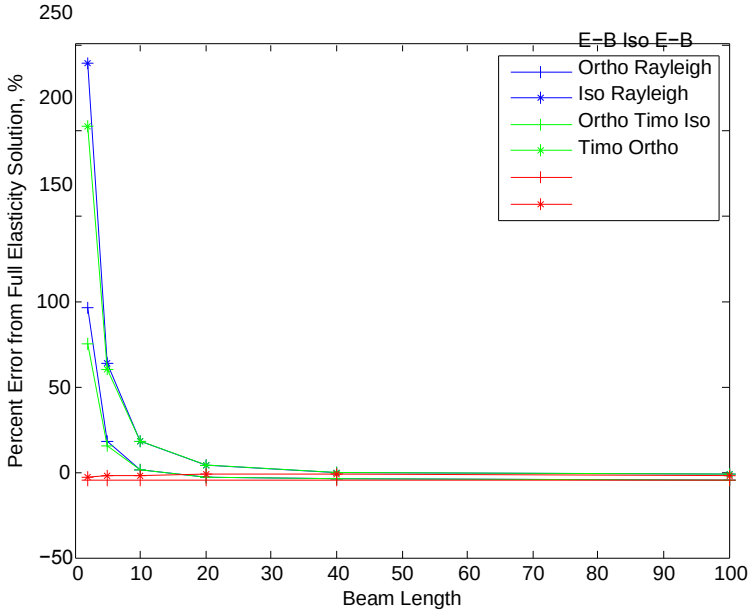

Figure 4.14 Error Comparison Between Isotropic and Orthotropic Materials for a Fixed-Fixed Beam

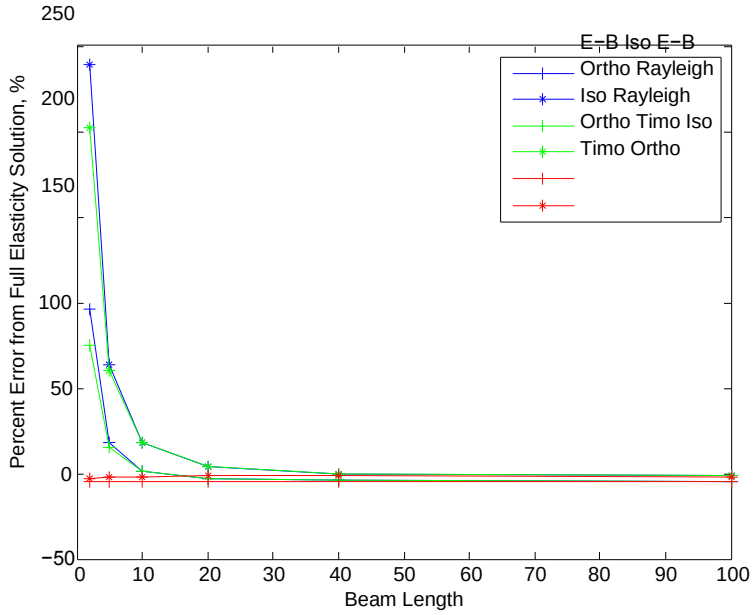

Figure 4.15 Error Comparison Between Isotropic and Orthotropic Materials for a Simply Supported Beam

The error increase for both the Euler-Bernoulli and Rayleigh beam theories is consistent throughout the different support conditions investigated for this study. The percent by which the frequency error increases varies slightly for the three cases, but in general the trend is consistent. For the Euler-Bernoulli and Rayleigh beam theories, the effect of an anisotropic material significantly amplifies the influence of low slenderness upon the accuracy of frequency results. For the Timoshenko model, the shear coefficient allows for the inclusion of anisotropic properties and thus provides similar results to isotropic beams for all three support cases. If the impacts of slenderness and anisotropy were the only considerations, it seems as if the Timoshenko model would be a reasonable approximation of frequency results for even very stout orthotropic beams. These two effects cannot be isolated though, and all three models result in significant error values for all slenderness values if at least one of the beam supports is fixed. The primary cause for this accuracy problem is most likely due to neglecting the Poisson effect, which will be discussed in the next section.

4.3.3 Effects of Poisson Ratio

The most unexpected result from this vibrational mechanics study is the significant difference between the Ritz-based elasticity method and the three beam theories for even very slender beams when at least one support in a beam is fixed. When these large errors were discovered, the suggested cause was the assumption of zero Poisson ratio in the typical beam theories. When considering a three-dimensional model, a perfectly fixed support completely restricts the Poisson effect. For example, in a cantilevered beam, the largest forces would exist at the fixed support and thus, the influence of the Poisson effect would cause the beam to shrink or expand through the width to counteract the large axial compression and tension forces. A perfectly fixed end does not allow this though, so the displacements and forces cannot act as is expected by typical beam theories. With a hinged or free support, there is no restriction of the Poisson effect and the beam is free to displace and vibrate as expected without any unusual effects. Therefore, ignoring the Poisson effect in a beam with only free or hinged supports would have minimal effect on the accuracy of the frequency results. In order to investigate this theory, the more accurate Ritz-based elasticity program was used to determine frequency results with both the normal material properties listed in Table 4.1 as well as elastic stiffness values found using $\nu = 0$. This allowed for the influence of the Poisson effect to be isolated from the other factors that cause errors in the typical beam theories.

The results of this investigation show that a consistent error exists between the models with and without the Poisson effect that is independent of beam slenderness. This is displayed in Figure 4.16, where the error in the fundamental mode is near 4.7% for a cantilevered beam, 3.4% for a fixed-fixed beam, and 0% for a simply supported beam. The percent difference does vary somewhat with the length of the beam, but the change is minimal and does not seem to follow a persistent trend. The result for the simply-supported beam case followed expectations and showed that neglecting the Poisson effect has a minimal influence. This was also the result for a free-free beam, which was investigated prior to this study. The error results were somewhat surprising for the fixed-free and fixed-fixed support conditions. Both of these cases did show a considerable error for all slenderness values, which was predicted, but the expected result was that the error would be higher for the fixed-fixed case than for the cantilevered beam. It seemed that the influence of the Poisson effect would increase with more restriction at the supports, but this was not the case. The reason for this is unclear and more study would be required to understand why the error is greater for the fixed-free case than for a fixed-fixed beam.

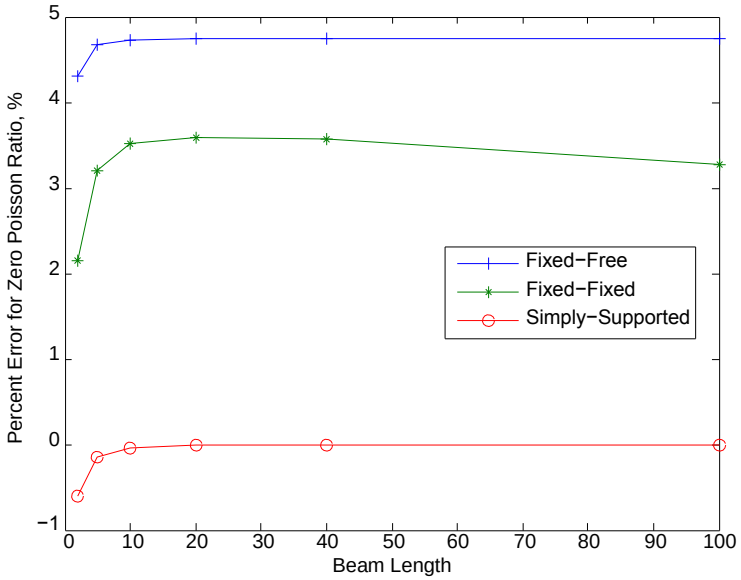

Figure 4.16 Influence of Poisson Effect for Varying Slenderness Ratios

Although the impact of neglecting the Poisson effect seems to be independent of slenderness, the error is related to the mode of vibration. Unexpectedly, the error decreased for higher modes of vibration for both cases including a fixed-support. It is uncertain why this is the case, and more investigation is necessary to determine the reason behind this pattern. For the simply supported case, the opposite pattern occurs. The influence of the Poisson effect is still minor for all modes of vibration, but the error does tend to increase for higher modes of vibration. These results are shown for a beam with a slenderness ratio of 69 in Figure 4.17.

The frequency error due to the Poisson ratio also appears to be connected with the material properties of a beam when a fixed support is present. The percent difference between the zero Poisson ratio and full elasticity results is far less for the orthotropic material studied than for the isotropic. The error is approximately six times greater for a steel beam than for a beam of graphite-magnesium if there is a fixed support. This result may be unique to these two materials, so other materials with both orthotropic and anisotropic properties would need to be studied to determine if the error is always less for an anisotropic solid. The results also show that this error difference does not exist for the simply supported beam. For this support case, the error values with or without the Poisson effect are virtually identical.

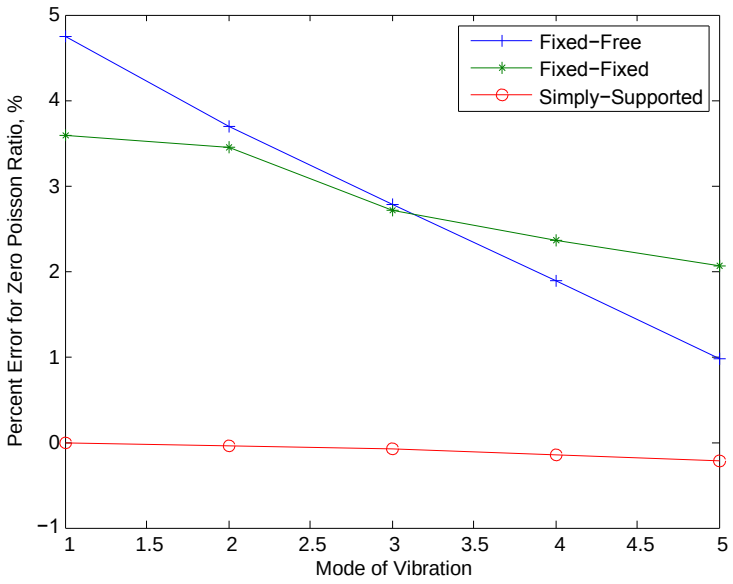

Figure 4.17 Influence of Poisson Effect for Varying Modes of Vibration

4.3.4 Conclusions

From the results discussed, a number of conclusions can be made. As previously stated, these results are only known for the geometry, materials, and constitutive laws that were used in the analysis. The determined findings are listed below.

1. For beams with at least one fixed support, the Timoshenko beam theory as well as an elasticity theory with zero Poisson ratio underestimate the frequency results. For very slender beams, the Euler-Bernoulli and Rayleigh beam theories also underestimate resonant frequencies, which contradicts expectations.

2. For a simply supported beam, all three beam theories and the zero Poisson condition overestimate frequency results. This occurs for all slenderness ratios and modes of vibration considered.

3. The slenderness ratio has a significant impact on the frequency accuracy for both the Euler-Bernoulli and Rayleigh beam theories. As the slenderness decreases, the error increases rapidly. This problem worsens for higher modes of vibration and anisotropic materials.

4. The resonant mode shapes for a non-slender beam deviate from one-dimensional beam theory predictions with significant warping through the thickness and height.

5. Neither slenderness nor anisotropy have a meaningful influence upon the frequency accuracy for the Timoshenko beam model.

6. None of the three studied beam theories provide acceptable results when a fixed support exists. In these cases, neglecting the Poisson effect leads to significant errors (more than 3%) for even extremely slender beams. When analyzing beams with fixed support conditions, more complex analysis, such as the full elasticity approximation used in this study, are necessary.

7. The influence of neglecting the Poisson effect decreases for higher modes of vibration with a cantilevered or fixed-fixed beam.

8. For beams with only hinged or free supports, the assumption of zero Poisson ratio has a minimal effect on the frequency results. This is true for both orthotropic and isotropic materials as well as all of the modes of vibration and slenderness ratios considered in this study.

The main purpose of this study was to determine when the typical beam theories are no longer acceptable. To summarize the answer to this investigation, all three theories are inadequate for beams with at least one fixed support regardless of slenderness or material type. For a simply supported beam, the Timoshenko beam model performs better than expected. The accuracy of frequency results only becomes poor for very low slenderness values combined with high modes of vibration. The Euler-Bernoulli and Rayleigh beam theories deteriorate in accuracy earlier than predicted. The common standard is that Euler-Bernoulli is acceptable for slenderness ratios greater than 100, but the results of this study contradict this. Even with a slenderness ratio of 138, the error for higher modes and orthotropic materials is near 2% for Euler-Bernoulli and above
1% for Rayleigh. The Timoshenko beam model is the clear choice for a simply supported beam unless the slenderness ratio is extremely high. For fixed-free or fixed-fixed beams, more complex analysis is required to calculate accurate resonant frequencies and mode shapes.

4.4 Method for Investigating MEMS Sensor

The calculation work performed for a proposed new MEMS sensor determined accurate estimates of resonant frequencies for certain modes of vibration. This device is planned to be an acoustic resonator with possible applications in molecular detection, strain sensing in civil infrastructure, and electronic frequency control. The primary sensing element of this device is a fixed-fixed bridge of silicon crystal with a thin film of gold. An illustration of the device, cross-sectioned through the middle, is provided in Figure 4.18. As the sensor experiences strain or mass loading from certain molecules, the resonant frequencies of this bridge will shift and be detected. For the application in structural health monitoring, the vision is that dynamic strains from both large-scale events, such as earthquakes and small-scale vibrations from acoustic emissions, could be detected and output. This device could also possibly be operated wirelessly, where the signal would be directly transmitted to a processing node. This would greatly reduce the complexity and cost over other available sensor systems.

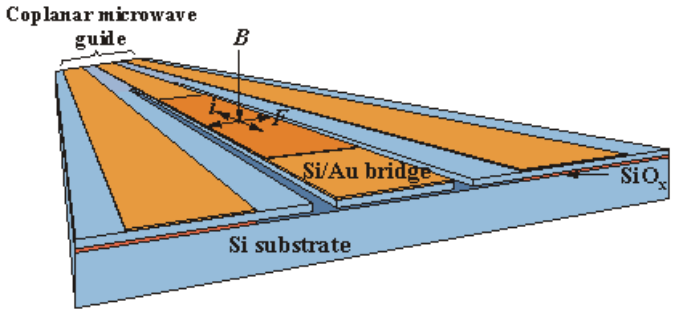

Figure 4.18 Illustration of MEMS Sensor Configuration Cross-Sectioned Through the Mid-Length

To proceed further with the development of this device, the inventor, Dr. Ward Johnson, will determine the exact resonant frequency range of the fixed-fixed bridge experimentally. Before this is feasible, more accurate estimates of these frequencies are needed they can be found experimentally. For the purpose of these estimates, the thin gold film will be neglected and only the properties of silicon will be input. Due to the results obtained from the vibration study discussed previously, the Ritz-based approximation program was utilized to calculate the resonant frequencies and mode shapes, since a higher error was found in all three beam theories when a fixed support was involved.

A few different bridge dimensions were analyzed in this work, with the length of the bridge varying. For all the cases, the width of the bridge is 69 microns and the thickness was set to 4.9 microns. Three different lengths were considered, since the best size in this dimension has not yet been decided. The three lengths studied were 400 microns, 600 microns, and 800 microns. The elastic constants and density used for the silicon material were determined by McSkimin and others and are provided in Table 4.8 [47]. These material properties and dimensions were input into the already created Ritz-based approximation program from the vibration study to determine resonant frequencies.

Table 4.8 Material Properties for Silicon

Constant	Value
C_{11}, GPa	167.4
C_{44}, GPa	65.23
C_{12}, GPa	79.57
Density, ρ, kg/m^3	2331

The modes of vibration, which are of particular interest for the operation of the device, are the lateral-flexural modes. The frequencies of lateral modes are more attractive because they experience less damping, which would lead to greater frequency resolution and sensitivity. The damping is lower for these modes than for transverse modes because less air or liquid is displaced through the movement, and thus less energy losses [48]. The Ritz-based approximation program was easily able to isolate the lateral-flexural modes of the bridge by simply selecting proper axes orientation. The computing program uses set displacement patterns for each axis, which are based upon the assumption of vertical or transverse displacement. By simply rotating the dimensions of the silicon beam so that the width dimension was vertical, the lateral modes were found. The determined resonant frequencies and mode shapes are discussed in the following section.

The developer of this device is also interested in determining the frequencies for the through-thickness shear modes for the silicon bridge. These vibration modes would disturb less air than the lateral flexural modes and would thus experience less damping and provide even greater frequency resolution. A simple diagram of the cross section deformation for this type of vibration is displayed in Figure 4.19. The calculations for the resonant frequencies of these mode types have not yet been completed. All other calculation work and investigations for this study focus on flexural vibrations, which have been studied in more depth, and thus, switching to shear mode calculations is a greater challenge than determining the lateral flexural modes. The hope is that these calculations can be completed soon and provide another option for the development of this new sensor.

4.5 Results from MEMS Sensor Investigation

Through the use of the Ritz-based approximation program for a fixed-fixed beam, the resonant frequencies for the first five lateral-flexural modes were determined. The values for these results are provided in Table 4.9. The fundamental lateral-flexural mode is of greatest interest for the development of the device, but higher modes were also calculated in case the need arose for these frequency estimations.

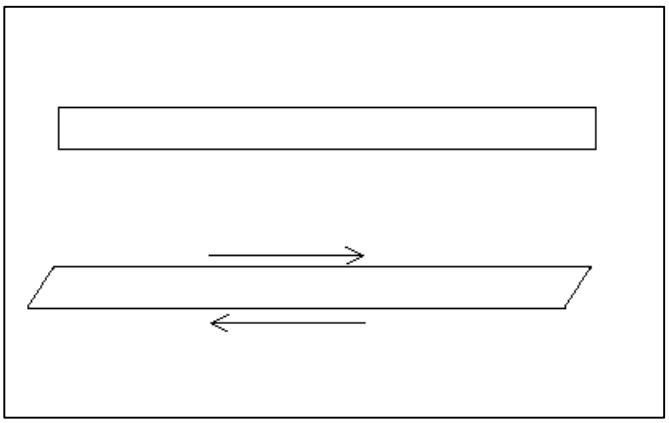

Figure 4.19 Illustration of Cross Section Deformation for Through-Thickness Shear Mode

Table 4.9 First Five Lateral-Flexural Mode Frequencies for MEMS Bridge

Length (microns)	Mode	Frequency (rad/s)
400	1	18225324
	2	44972102
	3	78724660
	4	116570326
	5	158118357
600	1	8548456
	2	22215588
	3	40562569
	4	62399670
	5	86980150
800	1	4908432
	2	13058480
	3	24389408
	4	38414047
	5	54548071

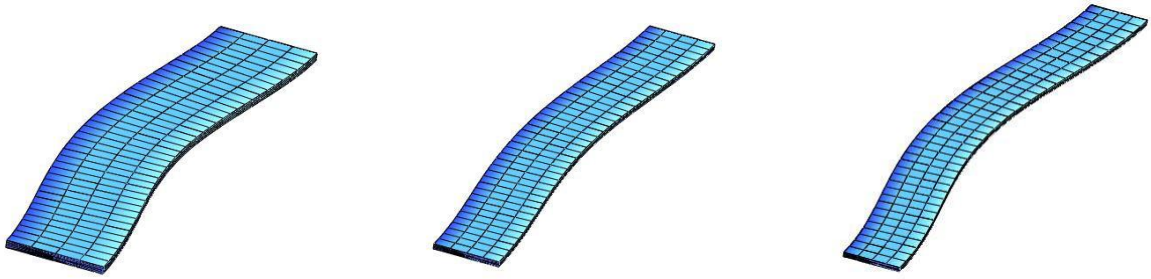

(a) 400 microns (b) 600 microns (c) 800 microns

Figure 4.20 Lateral-Flexural Vibration Modes for MEMS Bridge

Three-dimensional mode shapes for the fundamental lateral-flexural modes were plotted for each of the three lengths of interest. This was done to ensure that the frequencies calculated were for the correct vibrational modes of interest. These mode shapes are shown in Figure 4.5. The calculated mode shapes followed expectations and were confirmed to match the vibrational modes of interest for the MEMS sensor. With this information, the hope is that exact resonant frequencies can more easily be determined experimentally from the accurate estimations. This will advance the development and testing process for the device, which could potentially provide significant applications and advantages in cell sensing and structural health monitoring.

5. CONCLUSIONS

5.1 Summary of Work and Results

The bridges and buildings that the nation depends upon daily to provide safe and efficient usage, continually deteriorate from harsh environmental conditions and operational loads. Many of these structures have been in service for decades and are at risk of significant damage and deficiency. The field of structural health monitoring has arisen to attempt to prevent catastrophic failures and prioritize the immense amount of repair and maintenance that is required through persistent monitoring of the strength and integrity of a structure. Although many methods and technologies have been proposed and developed for the practice of structural health monitoring, a need still exists for further improvements to increase the applicability and affordability.

The research for this study aimed to contribute to possible advancements in the monitoring of civil infrastructure through three main goals. The first of these was to provide a thorough review of the concepts, methods, and technologies currently in use for structural health monitoring. This review presented the objectives of this practice and explained the theory behind multiple methods that have been established to fulfill these goals. Throughout these explanations, the benefits and drawbacks of each method were discussed and compared. This survey also offered the details of numerous sensor options that are available to obtain the data required to perform the analysis component of structural health monitoring. The concepts utilized for each of these technologies, their application capabilities, advantages, and disadvantages, were all presented. The motivation behind this overall review was to provide a general understanding of the field that could better direct further research. The primary motivation for this was to aid calculations included in this report, but it is hoped it will guide others in their investigations and experiments as well.

The second objective of this paper was to perform an in-depth study of vibrational beam mechanics theories to determine when and if their accuracy is unacceptable due to three key assumptions employed in all of them. This investigation was completed to ensure acceptable results could be obtained for calculations of a possible new structural health monitoring sensor. Three of the most common beam theories were considered: Euler-Bernoulli, Rayleigh, and Timoshenko. The Euler-Bernoulli model is the simplest option since it ignores the influences of the rotational inertia and shear forces in a beams displacement. The Rayleigh theory adds in rotary inertia, while Timoshenko includes both of these effects. All three theories assume the deformation occurs primarily in one dimension, the beam is relatively slender, the material is isotropic, and the Poisson effect is negligible. By employing an accurate Ritz-based elasticity approximation, each of these assumptions was tested to determine how it affects the accuracy of frequency and mode shape findings. Varying support conditions, beam lengths, and material properties were used in the analysis to better isolate each of the effects of interest. The conclusions of this investigation were compelling. A list of the key results found is provided below.

- When the slenderness ratio falls below 50, the errors in frequency results increases rapidly for both the Euler-Bernoulli and Rayleigh beam models, with errors up to 90% in one case.
- For higher modes of vibration and a slenderness ratio of 138, the frequency errors are above 2% for Euler-Bernoulli and Rayleigh, contradicting the assumption that these theories are adequate for beams with $s > 100$. This loss of accuracy for higher modes was consistent for all three beam cases.
- When the Euler-Bernoulli or Rayleigh theories are applied to an orthotropic material, the frequency errors for $s < 50$ more than double in comparison with the errors for an isotropic material. This trend was found for all three support cases.

- For all three support cases studied, the frequency errors for the Timoshenko model are not affected by very low slenderness or anisotropic properties.
- Due to neglecting the Poisson effect, none of the three beam theories are acceptable for beams with a fixed support since the frequency errors are 4% or greater for the entire range of slenderness values studied.
- When the influence of the Poisson ratio was isolated, it was found that neglecting this effect leads to frequency errors greater than 3% for beams with $s > 300$ when a fixed support exists.
- For the simply-supported case, the Poisson effect has a minimal influence, and it was found that the
  Timoshenko model gives excellent results for all slenderness ratios considered.

In summary, it was found that a more accurate, three-dimensional analysis should be utilized for beams involving a fixed support, but when this is not present, the Timoshenko model provides excellent results for all slenderness values, materials, and vibrational modes investigated.

The final and motivating goal of this work was to determine accurate estimates of resonant frequencies for the sensing component of a proposed MEMS sensor. This sensing component consists of a fixed-fixed, thin silicon bridge. Because of the support conditions of this bridge, the highly accurate three-dimensional elasticity solution used in the vibrational study was employed for the calculations. With this option available, accurate frequency estimates were obtained for the lateral-flexural modes of the bridge, which would aid in the experimental testing and development of this device.

5.2 Suggestions for Continued Research

Numerous opportunities exist for further research stemming from the work presented in this report. These research possibilities develop from two of the main goals of this study. First, there are multiple additional aspects that could be investigated to expand upon the vibrational mechanics study in this paper. Another assumption of typical beam theories is that the cross section of the beam is symmetrical, and it would be interesting to investigate beam dimensions that do not follow this parameter. Varying beam dimensions, in general, could be studied to better understand even the effects examined in this study. It is unclear if the existence of a fixed support would have as significant of an influence for non-square cross sections, hollow beams, and more, which could be of interest for multiple applications. Another option for further study would be to include a greater variety of material properties to further understand the effect of anisotropy on vibrational frequencies and mode shapes. More orthotropic materials could be included, as well as entirely anisotropic materials. Since the inclusion of a fixed support clearly had a meaningful impact on the action of a beam, a deeper investigation into the deformations, strains, and forces experienced at a fully fixed support could provide meaningful information to better understand this anomaly.

Another direction that additional research could go from the vibrational study presented would be to employ the more accurate three-dimensional elasticity approximation to applications that involve modal analysis and fixed supports. For example, there could be interest in how differently a structural frame modeled with fixed connections responds to modal analysis when the Poisson effect is included. Also, many MEMS devices that have been developed involve the response of a cantilevered beam, and the inclusion of the Poisson effect in their analysis could affect the results. A multitude of similar scenarios exist where a beam with a fixed support is involved, and which could benefit from applying the results found in this report.

Research possibilities could also follow the work done for the proposed MEMS sensor. Some research will likely occur by the developers to experimentally determine the actual resonant frequencies of the device and to decide which length for the silicon beam would provide the best operation. If the device has substantial potential, further work would be required to determine its accuracy in actually monitoring civil infrastructure. There is also potential for applicability in biomechanical fields such as cancer cell detection, and more research, testing, and development could also pursue this opportunity. In general, there are countless directions that new investigations could follow from this report and the hope is that the work presented here will provide a useful base from which to begin.

6. BIBLIOGRAPHY

[1] American Association of State Highway and Transportation Officials. *Bridging the Gap: Restoring and Rebuilding the Nation's Bridges.* 2008.

[2] U.S. Department of Transportation, Research and Innovative Technology Administration, Bureau of Transportation Statistics. *Transportation Statistics Annual Report 2010.* Washington, 2011.

[3] Doebling, Scott W., Charles R. Farrar, and Michael B. Prime. "A Summary Review of Vibration-Based Damage Identification Methods." *Shock and Vibration Digest.* 30.2 (1998):91-105.

[4] Farrar, Charles R., Scott W. Doebling, and David A. Nix. "Vibration-Based Structural Damage Identification." *Philosophical Transactions of the Royal Society.* 359. (2001):131-149.

[5] Doebling, Scott W., Charles R. Farrar, and Randall S. Goodman. "Effects of Measurement Statistics on the Detection of Damage in the Alamosa Canyon Bridge." 1997. 919-929.

[6] Chang, Peter C., Allison Flatau, and S.C. Liu. "Review Paper: Health Monitoring of Civil Infrastructure." *Structural Health Monitoring.* 2.3 (2003): 257-267.

[7] Alvandi, A. and C. Cremona. "Assessment of Vibration-Based Damage Identification Techniques." *Journal of Sound and Vibration.* 292. (2006):179-202.

[8] Cruz, Paulo J.S., and Rolando Salgado. "Performance of Vibration-Based Damage Detection Methods in Bridges." *Computer-Aided Civil and Infrastructure Engineering.* 24 (2008):62-79.

[9] Chong, Ken P., Nicholas J. Carino, and Gleen Washer. "Health Monitoring of Civil Infrastructures."
Smart Materials and Structures. 12. (2003):483-493.

[10] Gastineau, Andrew, Tyler Johnson, and Arturo Schultz. Minnesota Department of Transportation. *Bridge Health Monitoring and Inspection - A Survey of Methods.* 2009.

[11] Aktan, A. Emin, F. Necati Catbas, Kirk A. Grimmelsman, and Mesut Pervizpour. Federal Highway Administration Research and Development. *Development of a Model Health Monitoring Guide for Major Bridges.* 2003.

[12] Phares, Brent M., Terry J. Wipf, Lowell F. Greimann, and Yoon-Si Lee. Wisconsin Department of Transportation. *Health Monitoring of Bridge Structures and Components Using Smart-Structure Technology Volume 1.* 2005.

[13] Park, H.S., H.M. Lee, H. Adeli, and I. Lee. "A New Approach for Health Monitoring of Structures: Terrestrial Laser Scanning." *Computer-Aided Civil and Infrastructure Engineering.* 22.1 (2007):19-30.

[14] Wilson, Jon, Craig Aszkler, and Timothy Geiger. "Acceleration, Shock, and Vibration." *Test and Measurement: know it all.* Boston: Elsevier Inc., 2009. 101-151.

[15] *Introduction to Piezoelectric Accelerometers.* 2012. Graphic. PCB Piezotronics, Inc. 2 Apr 2012. <http://www.pcb.com/techsupport/tech_accel.php>.

[16] Choi, Haksoo, Sukwon Choi, and Hojung Cha. "Structural Health Monitoring System Based on Strain
Gauge Enabled Wireless Sensor Nodes." *5th International Conference on Networked Sensing Systems.*
211-214. 17-19 June 2008.

[17] Zou, Y., L. Tong, and G.P. Steven. "Vibration-Based Model-Dependent Damage (Delamination) Identi- fication and Health Monitoring for Composite Structures - A Review." *Journal of Sound and Vibration.* 230.2 (2000):357-378.

[18] Kesavan, Ajay, Sabu John, and Israel Herszberg. "Strain-based Structural Health Monitoring of Complex Composite Structures." *Structural Health Monitoring.* 7.3 (2008):203-213.

[19] Laughton, Michael, Douglas Warne and E.A. Parr. "Strain Gauges, Load Cells, and Weighing." *Test and Measurement: know it all.* Boston: Elsevier Inc., 2009. 267-280.

[20] *The Strain Gauge.* 2007. Automatic Control, Robot and Mechatronics Labs of Mechanical Engineering Department. Web. 3 Apr 2012. <http://web.deu.edu.tr/mechatronics/TUR/strain gauge.html>.

[21] Watkins, S., J. Fonda and A. Nanni. "Assessment of an Instrumented Reinforced Concrete Bridge with
Fiber-Reinforced Polymer Strengthening." *Optical Engineering.* 46.5 (2007).

[22] Ravisankar, K., S. Parivallal, T. Narayanan, K. Kesavan and R. Narayanan. "Vibrating Wire Strain Gauges for Long-Term Monitoring of Structures." *Indian Concrete Journal.* 75.8 (2001):535-541.

[23] Dally, J. and W. Riley. *Experimental Stress Analysis.* 4. Knoxville: College House Enterprises, 2005. [24] Neild, S.A., M.S. Williams and P.D. Mcfadden. "Development of a Vibrating Wire Strain Gauge for Measuring Small Strains in Concrete Beams." *Strain.* 41.1 (2005):3-9.

[25] Domalik, D., J. Shura and D. Linzell. "Design and Field Monitoring of Horizontally Curved Steel Plate Girder Bridge." *Transportation Research Record.* (2005):83-91.

[26] *Vibrating Wire Strain Gages.* 2011. Photograph. CARBO Ceramics. 2 Apr 2012. <http://www.carboceramics.com/agi/strain-gauges>.

[27] Corda, J. and L.K. Al-Tayie. "Enhanced Performance Variable-Reluctance Transducer for Linear-position Sensing." *IEE Proceedings: Electrical Power Applications.* 150. (2003):623-628.

[28] McDonald, P.C. and C. Iosifescu. "Use of LVDT Displacement Transducer in Measurements at Low
Temperatures." *Measurement Science and Technology.* 9.4 (1998):563-569.

[29] Fischer-Cripps, Tony. "Position." *Test and Measurement: know it all.* Boston: Elsevier Inc., 2009. 255-265.

[30] *Tilt Measuring - Inclinometers - Levelling.* 2012. Graphic. ALTHEN Mess - und Sensortechnik, Frankfurter. 3 Apr 2012. <http://www.althensensors.com/inclinometer and tilt sensors/ait930>.

[31] Vallen, Hartmut. “AE Testing Fundamentals, Equipment, Applications.” *NDT.net* 7.9 (2002).

[32] Casas, J. and P. Cruz. “Fiber Optic Sensors for Bridge Monitoring.” *Journal of Bridge Engineering.* 2.3 (2003):257-267.

[33] Yin, S., P. Ruffin and F. Yu. *Fiber Optic Sensors.* 2nd edition. Boca Raton: CRC Press, 2008.

[34] Inaudi, D. and S. Vurpillot. “Monitoring of Concrete Bridges with Long-Gage Fiber Optic Sensors.”
Journal of Intelligent Material Systems and Structures. 10.4 (1999):280-292.

[35] Ozevin, D., D.W. Greve, I.J. Oppenheim, and S.P. Pessiki. “Resonant capacitive MEMS acoustic emission transducers.” *Smart Materials and Structures.* 15.6 (2006):1863-1871.

[36] Mohammed, A.A.S., W.A. Moussa and E. Lou. “A novel MEMS strain sensor for structural health monitoring applications under harsh environmental conditions.” *Structural Health Monitoring 2007: Quantification, Validation, and Implementation.* Ed. F.K. Chang. Lancaster: DEStech Publications, Inc., 2007. 121-128.

[37] Rajagopalan, Jagannathan and M. Taher A. Saif. “MEMS sensors and microsystems for cell mechanobiology.” *Journal of Micromechanics and Microengineering.* 21.5 (2011).

[38] Gao, Song and Xinyan Wang. “Microelectromechanical system-based diagnostic technology for cervical cancer.” *Journal of Cancer Research and Clinical Oncology.* 137.11 (2011):1721-1727.

[39] Han, S.M., H. Benaroya, and T. Wei. “Dynamics of Transversely Vibrating Beams Using Four Engineering Beam Theories.” *Journal of Sound and Vibration.* 225.5 (1999):935-988.

[40] Timoshenko, S.P. *History of Strength of Materials*. New York: McGraw-Hill Book Company, Inc., 1953.

[41] Timoshenko, S.P. “On the correction for shear of the differential equation for transverse vibrations of bars of uniform cross-section.” *Philosophical Magazine.* 41. (1921): 744-746.

[42] Fung, Y.C., & Tong, P. *Classical and Computational Solid Mechanics*. Hackensack: World Scientific
Publishing Co. Pte. Ltd., 2010.

[43] Puchegger, S., D. Loidl, K. Kromp, and H. Peterlik. “Hutchinson’s Shear Coefficient for Anisotropic Beams.” *Journal of Sound and Vibration.* 266. (2003):207-216.

[44] Heyliger, P.R., and A. Jilani. “The Free Vibrations of Inhomogeneous Elastic Cylinders and Spheres.” *Int. J. Solids Structures.* 29.22 (1992):2689-2708.

[45] Ohno, Ichiro. “Free Vibration of a Rectangular Parallelepiped Crystal and its Application to Determination of Elastic Constants of Orthorhombic Crystals.” *Journal of Physics of the Earth.* 24. (1976)355-379.

[46] Ledbetter, H.M., S.K. Datta, and T. Kyono. “Elastic Constants of a Graphitemagnesium Composite.” *Journal of Applied Physics.* 65:9. (1989):3411-3416.

[47] McSkimin, H.J., W.L. Bond, E. Buehler and G.K. Teal. "Measurement of the Elastic Constants of Silicon Single Crystals and Their Thermal Coefficients." *Physical Review*. 83.5 (1951):1080-1080.

[48] Heinrich, S.M., R. Maharjan, I. Dufour, F. Josse, L.A. Beardslee and O. Brand. "Analytical Model of a Thermally Excited Microcantilever Vibrating Laterally in a Viscous Fluid." *IEEE Sensors 2010 Conference*. 1399-1404. Nov 2010.